NASA CR-

Hypervelocity Impact - A Series Solution Part II - Spherical Flow TR #65-16 June 1965

HYPERVELOCITY IMPACT - A SERIES SOLUTION

PART II - SPHERICAL FLOW

By Paul Marnell and Melvin Zaid

By: Technik Incorporated
50 Jericho Turnpike
Jericho, New York

TR #65-16
June 1965

For: N.A.S.A.
Langley Research Center
Hampton, Virginia

Contract No. NAS1-2622

CONTENTS

NOMENCLATURE

a	initial crater radius, ft
b	computational quantity defined by Equation (A25)
$b_0, b_1, \ldots$	coefficients of the $b(\epsilon)$ series
c	adiabatic bulk sonic velocity, ft/sec
C_1, C_2	R_1 solution constants defined by Equation (A63)
D	equivalent spherical diameter of penetrator, as defined by Equation (52), ft
$\mathbb{D}$	computational quantity used in specifying I_1, I_2, and I_3
e	internal energy, ft-lbf/ft^3
f	parameter introduced in evaluating ρ_0 (m, t) (see Equation (A33))
$f_1(g), f_2(g)$	computational quantities defined by Equations (A49) and (A51)
g	generalized time $\left(g \equiv 1 + \frac{4 v_0 t}{a}\right)$
G	computational quantity defined by Equation (A41)
h	generalized particle parameter $\left(h \equiv 1 + \left(\frac{12-3\beta}{4}\right)\frac{m}{\rho^\circ a^3}\right)$
H	Hugoniot function
I_1^*, I_2^*, I_3^*	computational quantities defined by Equations (A44), (A45), and (A46)
I_1, I_2	Computational quantities defined by Equations (A66) and (A67)
J_2'	Computational quantity defined by Equation (A68)
J_2	computational quantity used in specifying I_1, I_2, and I_3
K_2, K_3	parameters introduced in evaluating R_1 (see Equations (A41) and (A52))
L	modified plane case penetrator length, ft
$l_1, l_2, \ldots, l_7$	R_1 solution constants defined by Equation (A58)
$L_1, L_2, \ldots, L_7$	R_1 solution constants defined by Equation (A60)
$\mathcal{L}_1, \mathcal{L}_2, \ldots, \mathcal{L}_7$	R_1 solution constants defined by Equation (A59)
m	Lagrangian particle parameter $\left(m \equiv \frac{\rho^\circ}{3}(r^{\circ 3} - a^3)\right)$, slug
m_p	penetrator mass, slug
m_t	impacted target layer mass, slug

M_P	modified-penetrator mass ($M_P \equiv m_P + m_T$), slug
n	integer value, 0, 1, ...
p	pressure, lbf/ft^2 (sometimes in megabars)
P	depth of penetration (crater radius), ft
q	kinetic energy fraction (see p. 6 for definition)
r	radial coordinate, ft
R	shock radius, ft
s	constant in Hugoniot velocity relationship, see Equation (19)
t	time, sec
u	particle velocity, ft/sec
V	magnitude of impact velocity, ft/sec
$\underline{V}$	impact velocity vector, ft/sec
v	impact particle velocity, ft/sec
$v_0, v_1, \ldots$	coefficients of the $v(\epsilon)$ series, ft/sec
X	modified-penetrator radius, ft
x, y, z	cartesian coordinates, ft
α	penetration-velocity relationship exponent ($P/D \propto V^{\alpha}$)
β	R_1 solution constant defined by Equation (A61)
γ	adiabatic exponent
γ_1	parameter introduced in evaluating R_1 (see Equation (A41))
δ	R_1 solution constant defined by Equation (A62)
ϵ	impact density ratio ($\epsilon \equiv \rho^o/\rho^*_{IMPACT}$)
θ_0, θ_1	computational quantities defined by Equations (33) and (36)
κ	Hugoniot exponent
ν	parameter introduced in evaluating R_1 (see Equation (A43))
ρ	density, slug/ft^3

σ^* dynamic yield stress, lbf/ft^2 or megabar

τ time at which a particle becomes shocked when $\epsilon \approx 0$, sec

Superscripts

o pre-impact

* shock front

Subscripts

H Hugoniot

C crater

P penetrator

LIST OF FIGURES

LIST OF TABLES

1. INTRODUCTION

1.1 Background

In Part I of this report, an infinite series technique for analytically describing the hydrodynamic phase of the hypervelocity impact process is developed and applied to the case of a one-dimensional impact under the assumptions of a rigid penetrator and a constant shock density. The application of the method to the more general case of spherical target flow with a compressible penetrator and a variable shock density is treated herein.

The purpose of the one-dimensional study is the demonstration of the feasibility of the series solution technique. As such, several important physical effects (geometric divergence of the flow-field, penetrator compressibility, and shock density variation) were not considered initially in order to concentrate on the fundamental aspects of the solution technique with as simple a model as possible. Having established the usefulness of the method, it is now extended to include the effects necessary to yield a physically detailed, analytical description of the hydrodynamic phase of hypervelocity impact.

1.2 Objectives

The objectives of the Part II analysis are:

1. An analytical series solution of the hydrodynamic phase of impact based on a model which includes:
    a. spherical target flow
    b. penetrator compressibility
    c. variable shock density
2. A determination of the relationship between infinite target crater depth

and impact velocity based on the derived series solution.

1.3 Approach

The spherical impact of a compressible penetrator and an infinite target is investigated utilizing the infinite series technique developed in Part I. As before, ideal fluid behavior is assumed throughout the variable shock flow process. Target strength is introduced as a final condition to terminate the crater growth.

2. ANALYSIS

2.1 Theoretical Model

2.1.1 Physical Basis

The physical basis for the theoretical model to be discussed is illustrated by the impact crater shown in Figure 1a. The significant features of the impact (aluminum on copper) are the hemispherical nature of the crater and the fairly uniform coating of the penetrator over the crater surface, both of which are consistent with the fluid dynamic picture of hypervelocity impact. As the pressure and temperature levels decay with time, strength becomes a major factor in controlling the flow of target and projectile material. Eventually the flowing material "freezes" due to the onset of internal resistive forces which limit gross macroscopic flow.

All craters are not as symmetric and uniformly coated as that pictured in Figure 1a. In certain instances the penetrator may mix with the target crater material, a phenomena which occurs when copper impacts aluminum, as shown in Figure 1b. This latter effect may be related to a flow instability arising from the relative differences in density between the penetrator and target. In this investigation the more regular type of behavior of Figure 1a will be examined.

2.1.2 Physical Idealization

2.1.2.1 Instant of Impact

Based on the preceding considerations, the instant of impact is idealized as shown in Figure 2. It is assumed that immediately upon impact the penetrator and a layer of impacted target material form two concentric flowing

(1a) Aluminum on Copper

(1b) Copper on Aluminum

Fig. 1. Examples of typical hypervelocity impact craters.

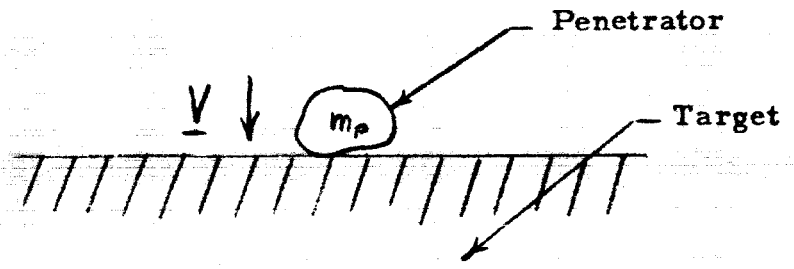

SYSTEM AT IMPACT

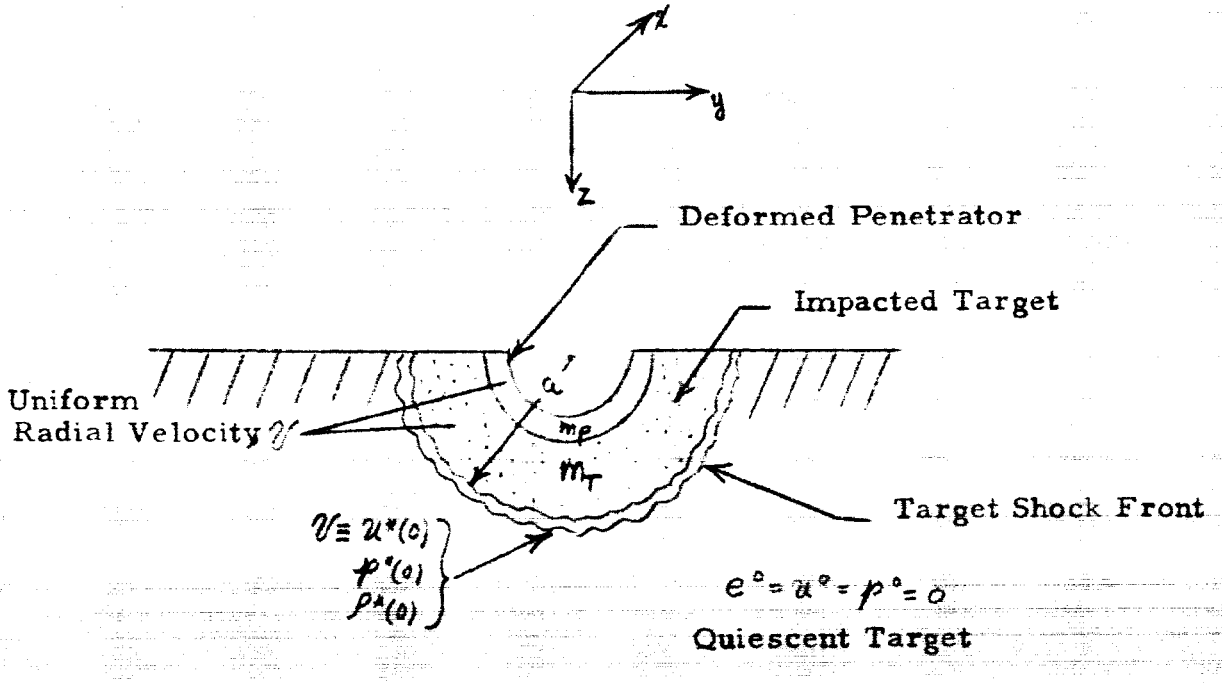

IDEALIZED SYSTEM JUST AFTER IMPACT

Fig. 2. The idealization of the penetrator-target system at the instant of impact.

hemispherical shells. The particle velocity (which is purely radial) and pressure within each shell are uniform; their values are equal to those at the impacted target layer shock front,

$$\mathcal{V} \equiv u_{IMPACT} = u^*(0) \tag{1}$$

$$p_{IMPACT} = p^*(0). \tag{2}$$

Application of the momentum and energy conservation laws yields unique values for the impacted target layer mass, m_T, and the impact particle velocity which are consistent with the postulated flow-field. Thus, using the notation of Figure 2, conservation of momentum in the z direction requires that

$$m_P V = m_P \frac{\mathcal{V}}{2} + m_T \frac{\mathcal{V}}{2}, \tag{3}$$

the factor of 1/2 on the right side of the equation arising from the fact that the deformed penetrator and impacted target layer are flowing radially.
Energy conservation necessitates that

$$m_P \frac{V^2}{2} = m_P \frac{\mathcal{V}^2}{2} + m_T \frac{\mathcal{V}^2}{2} + (1-\beta)\, m_P \frac{V^2}{2}, \tag{4}$$

where β (defined as the "kinetic energy fraction") is the fraction of the initial penetrator kinetic energy which appears as deformed penetrator and impacted target layer kinetic energy.* Equations (3) and (4) can be solved for m_T, the impacted target layer mass, and $\mathcal{V}$, the impact particle velocity. Thus,

$$\mathcal{V} = \frac{\beta}{2} V \tag{5}$$

$$m_T = \left(\frac{4}{\beta} - 1\right) m_P. \tag{6}$$

* β is assumed independent of the penetrator kinetic energy.

Since, for this model, there is no loss of target mass, the initial crater radius follows as

$$\frac{2}{3}\pi a^3 \rho^\circ = m_T = \left(\frac{4}{\beta} - 1\right) m_p \qquad (7a)$$

or

$$a = \left(\frac{3 m_p}{2\pi\rho^\circ}\left[\frac{4}{\beta} - 1\right]\right)^{1/3}. \qquad (7b)$$

It should be emphasized that the effects of penetrator compressibility and material properties at the instant of impact are accounted for in this formulation. Thus, β can be obtained from a rigorous analysis of the one-dimensional impact between infinite slabs, one of the target material and one of the penetrator material.[2] For example, for similar material impact, $\beta = 1/2$. With β calculated in the manner, Equations (5), (6), and (7) give a reasonable representation of the state of affairs existing at impact. (For a one-dimensional impact, the model would be perfectly rigorous. Physically, it would depict the situation existing at the instant that the penetrator shock reaches the back face of the penetrator.)

2.1.2.2 After Impact

As just shown, there is a unique impacted target layer mass, impact particle velocity, and initial crater radius associated with the postulated initial impact flow-field. At the instant of impact, the flow-field shown in Figure 2 is equivalent to that which would arise if a "rigid" hemispherical shell (defined as a "modified-penetrator") with a mass

$$M_p \equiv m_p + m_T = \frac{1}{\beta} m_p = \frac{8\pi a^3 \rho^\circ}{12 - 3\beta}, \qquad (8)$$

initial outer radius a, and uniform radial velocity V impacted a target with initial crater radius a (see Figure 3a). The modified-penetrator is "rigid"

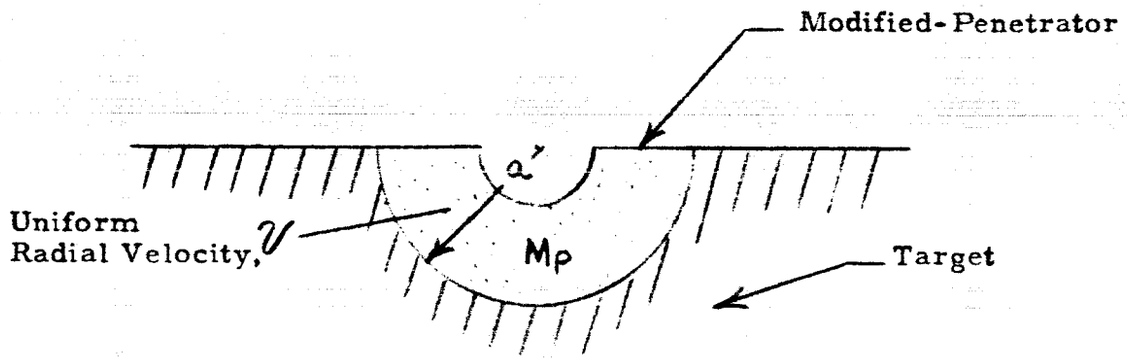

(3a) AT IMPACT

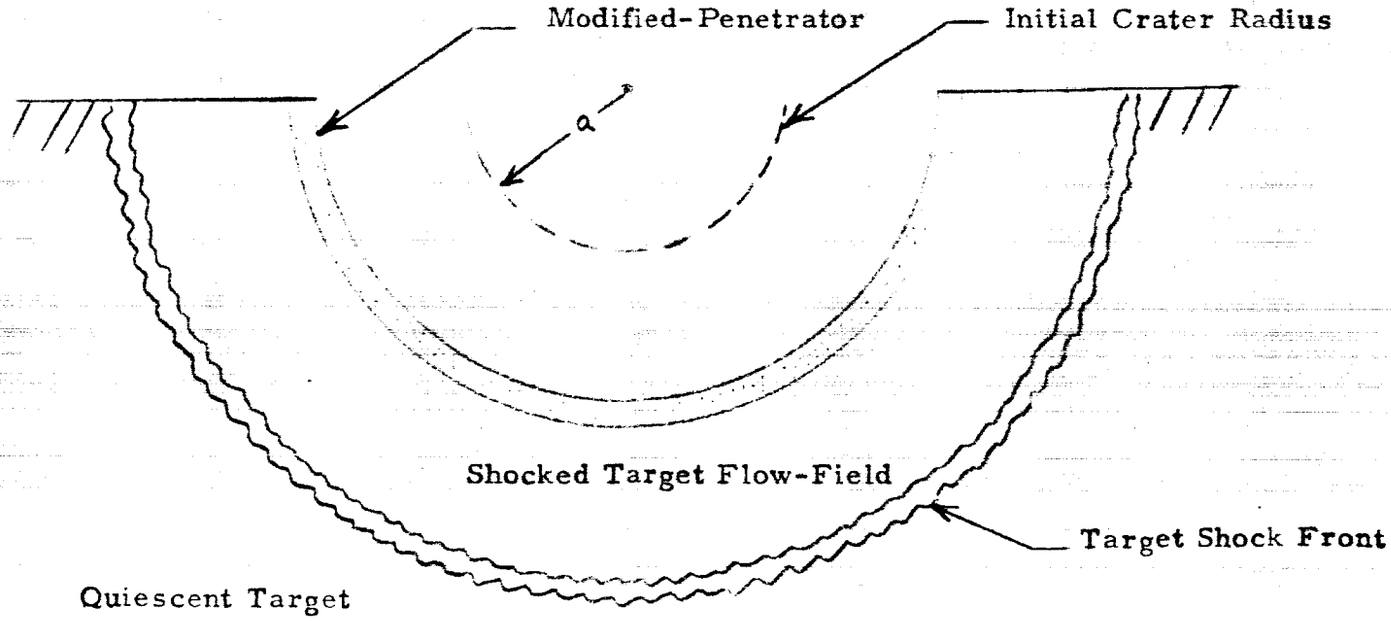

(3b) AFTER IMPACT

Fig. 3. The modified-penetrator idealization for all times after impact.

in the sense that the initial particle velocity over the hemispherical impact surface is V , the impact velocity of the modified-penetrator.*

It is postulated that for all succeeding times after impact the modified-penetrator acts as a deformable, hemispherical shell piston which is in constant bearing contact with the target (see Figure 3b). Its velocity distribution is always radial. For purposes of computing its equation of motion, the velocity of the target-modified-penetrator hemispherical interface is taken to be that of the modified-penetrator center-of-mass. As discussed in Part I (see Section 3.4.2) this latter approximation should be of higher-order significance.

2.2 Mathematical Formulation

2.2.1 Fluid Dynamic Equations

As in the one-dimensional analysis, it is assumed that

1. The flow is inviscid and adiabatic; real fluid effects, i.e., viscosity and heat transport, are absent except in the advancing target shock front.
2. Strength effects are negligible during the flow process.**
3. The adiabatic pressure-density relationship is given by

$$p\rho^{-\gamma} = \text{CONSTANT}. \tag{9}$$

For the assumed spherical flow-field, it is also convenient to use the Lagrangian form of the fluid dynamic equations. The particle parameter is now defined as

$$m \equiv \frac{\rho^0}{3}\left[r^{0^3} - a^3\right], \tag{10}$$

*In the rigid penetrator, one-dimensional analysis, the initial particle velocity $u(0,0)$ is equal to the impact velocity of the penetrator, V.
**Strength is considered, however, in evaluating the final crater radius.

where ρ° and r° are the undisturbed target density and initial radius of the particle, respectively. (Figure 4 illustrates the flow-field geometry notation.) The Lagrangian form of the fluid dynamic equations appropriate for spherical flow is [3]

Continuity:
$$\frac{\partial r}{\partial m} = \frac{1}{r^2 \rho} \tag{11}$$

Momentum:
$$\frac{\partial^2 r}{\partial t^2} = -r^2 \frac{\partial p}{\partial m} \tag{12}$$

Energy:
$$\frac{\partial}{\partial t}(p \rho^{-\gamma}) = 0. \tag{13}$$

Equations (11) and (12) differ from their one-dimensional counterparts (Equation (30) and (31) of Part I) in the $\frac{1}{r^2}$ factor which accounts for spherical divergence of the **pressure and velocity fields.**

2.2.2 Boundary and Initial Conditions

2.2.2.1 Initial Conditions

From the idealization of Section 2.1, at the instant of impact the radius of the modified-penetrator, target crater, and shock front are all equal to a. The initial velocity of the modified-penetrator is the impact particle velocity. Thus,

$$r(0,0) = X(0) = R(0) = a \tag{14}$$

$$\left.\frac{\partial r}{\partial t}\right|_{0,0} = \dot{X}(0) = V. \tag{15}$$

2.2.2.2 Boundary Conditions

Target-Modified-Penetrator Interface

The flow is spherical; hence, only the z-component of the modified-penetrator momentum is different from zero. The rate of change of this

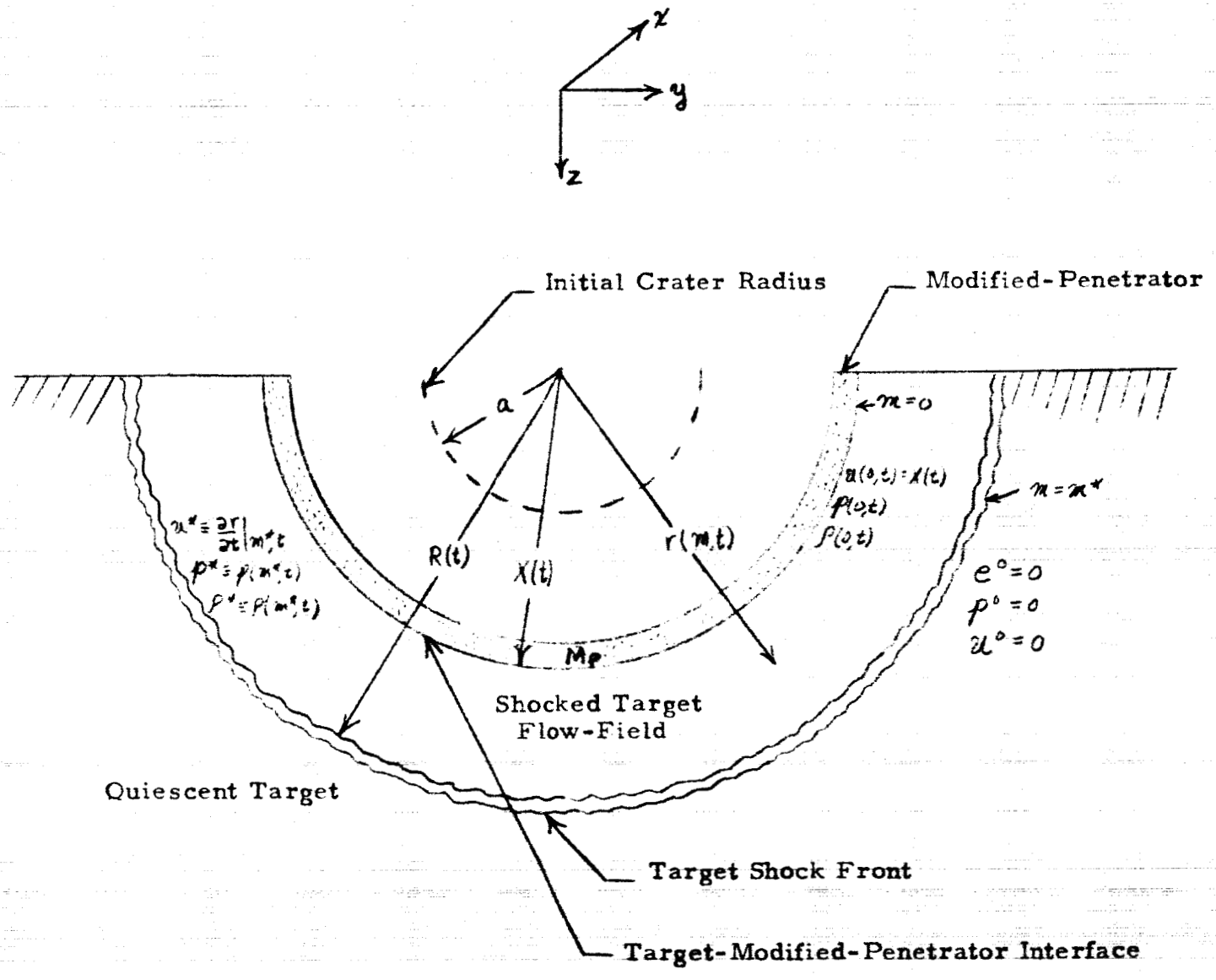

Fig. 4. The Lagrangian representation of the spherical flow-field.

momentum is governed by the z-component of the pressure force acting at the target-modified-penetrator interface. Thus,

$$M_p \frac{\ddot{X}}{2} = -p(0,t)\pi X^2. \tag{16}$$

Since

$$r(0,t) = X(t), \tag{17}$$

it follows that

$$\left.\frac{\partial^2 r}{\partial t^2}\right|_{0,t} = -\frac{2\pi r^2(0,t)\, p(0,t)}{M_p}. \tag{18}$$

Target Shock Front

The shock density is treated as a time varying quantity. From the experimentally derived shock velocity expression

$$u^* \equiv u(m^*,t) = \frac{\dot{R}-c}{s}, \tag{19}$$

and the rigorous shock pressure relationship $p^* = \rho^o u^* \dot{R}$, it follows that

$$p^* \equiv p(m^*,t) = \frac{\rho^o}{s}(\dot{R}^2 - c\dot{R}). \tag{20}$$

The form of the corresponding shock density equation, $\frac{1}{\rho^*} = \frac{1}{\rho^o}\left\{1-\left[\frac{1}{s}\left(1-\frac{c}{\dot{R}}\right)\right]\right\}$, does not allow for a series representation. A form which does yield a series expansion and which is a good approximation to the pressure-density variation along a Hugoniot curve[4]** is

$$p^* \rho^{*-\kappa} = (p^* \rho^{*-\kappa}), \tag{21}$$

where κ is generally larger than the adiabatic exponent γ.*

* It should be emphasized that Equations (9) and (21) represent two distinct phenomena. Equation (9) refers to the pressure-density relationship of a given particle during adiabatic expansion. Equation (21) relates the shock density to the shock pressure as the shock front moves into the target.
**Hugoniot data for various metals is given in Reference 5.

Equations (19), (20), and (21) are three equations for the shock velocity, pressure, and density which account for the variable shock density.

2.3 Method of Solution

The solution of Equations (11), (12), and (13) subject to the initial and boundary conditions specified by Equations (14), (15), (18), (19), (20) and (21) is presented in this section. Analytical details are presented in the Appendix.

2.3.1 Series Expansions

In complete analogy with the one-dimensional analysis, it is assumed that the flow-field distributions can be expanded in terms of powers of the impact density ratio, ϵ , defined as

$$\epsilon \equiv \frac{\rho^{\circ}}{\rho^{*}_{IMPACT}} , \tag{22}$$

where ρ^{*} is the density of the initial impacted target layer described in Section 2.1. Thus, for a specified target material and penetrator mass we seek solutions of the form

Particle Position: $$r(m,t,\epsilon) = \sum_{n=0}^{\infty} r_n(m,t)\epsilon^n \tag{23}$$

Shock Position: $$R(t,\epsilon) = \sum_{n=0}^{\infty} R_n(t)\epsilon^n \tag{24}$$

Modified-Penetrator Position: $$X(t,\epsilon) = \sum_{n=0}^{\infty} X_n(t)\epsilon^n \tag{25}$$

Pressure: $$p(m,t,\epsilon) = \sum_{n=0}^{\infty} p_n(m,t)\epsilon^n \tag{26}$$

Density: $$\rho(m,t,\epsilon) = \sum_{n=0}^{\infty} \rho_n(m,t)\epsilon^{n-1} . \tag{27}$$

2.3.2 Coefficient Differential Equations

Substitution of Equations (23), (26), and (27) into Equations (11), (12), and (13) yields a system of partial differential equations for the coefficients in the flow variable series. For the zeroeth and first-order coefficients we have

$$\frac{\partial r_0}{\partial m} = 0 , \qquad \frac{\partial r_1}{\partial m} = \frac{1}{\rho_0 r_0^2} , \tag{28a,b}$$

$$\frac{\partial^2 r_0}{\partial t^2} = -r_0^2 \frac{\partial p_0}{\partial m} , \qquad \frac{\partial p_1}{\partial m} = \frac{1}{r_0^2}\left(\frac{2\ddot{r}_0 r_1}{r_0} - \frac{\partial^2 r_1}{\partial t^2}\right) , \tag{29a,b}$$

$$\frac{\partial}{\partial t}\left(p_0 \rho_0^{-\gamma}\right) = 0 , \qquad \frac{\partial}{\partial t}\left(\frac{p_1}{p_0} - \frac{\gamma \rho_1}{\rho_0}\right) = 0 . \tag{30a,b}$$

These equations are readily integrable. Thus,

$$r_0(m,t) = r_0(t) \tag{31}$$

$$p_0(m,t) = -\frac{\ddot{r}_0}{r_0^2} m + p_0(0,t) \tag{32}$$

$$\rho_0(m,t) = \frac{p_0^{1/\gamma}}{\theta_0(m)} \tag{33}$$

$$r_1(m,t) = \int_0^m \frac{1}{\rho_0 r_0^2}\, dm + r_1(0,t) \tag{34}$$

$$p_1(m,t) = \frac{1}{r_0^2}\int_0^m \left(\frac{2\ddot{r}_0 r_1}{r_0} - \frac{\partial^2 r_1}{\partial t^2}\right) dm + p_1(0,t) \tag{35}$$

$$\rho_1(m,t) = \frac{\rho_0}{\gamma}\left(\frac{p_1}{p_0} + \theta_1(m)\right), \tag{36}$$

where $\theta_0(m)$ and $\theta_1(m)$ are functions of m to be specified by the boundary conditions.

Higher order terms can be calculated. However, experience with the one-dimensional solution indicates that the second-order contribution to a three term series is only about 5% shortly after impact. Hence, for the spherical flow analysis a similar relationship between the magnitude of the first 3 terms is postulated, so that only the first 2 series coefficients are evaluated.

2.3.3. Flow-Field Solution

2.3.3.1 Truncated Series Expansions

Following the procedure developed for the one-dimensional analysis, the series coefficients given by Equations (31) through (36) are obtained by applying the initial and boundary conditions and solving for the functions of integration

$$r_i(0,t),\ P_i(0,t),\ \theta_i(m) \qquad (i=0,1).$$

This procedure also yields R_0 and R_1, the first two shock position series coefficients.

The radial location of a fluid particle at the target-modified-penetrator interface is equal to that of the penetrator, i.e.,

$$r(0,t,\epsilon) = X(t,\epsilon)$$

$$r_0(t) + r_1(0,t)\epsilon + \cdots = X_0(t) + X_1(t)\epsilon + \cdots, \tag{37}$$

and, equating coefficients of like powers of ϵ

$$r_0(t) = X_0(t) \tag{38a}$$

$$r_1(0,t) = X_1(t) \tag{38b}$$

$$\vdots \qquad \vdots$$

Hence, as for the one-dimensional flow, the modified-penetrator position series coefficients are derivable from those of the particle position series.

The detailed evaluation of the various series coefficients is given in the Appendix. Table 1 presents the first two terms of the series expansions. As can be seen, to calculate the target flow-field for a given penetrator impact velocity, V, and mass, m_p, one needs only to specify the target's undisturbed density, ρ^o, adiabatic exponent, γ, Hugoniot exponent, χ, adiabatic bulk sonic velocity, c, and shock velocity constant, s, and the impact particle velocity-density ratio function $\mathcal{V}(\epsilon)$. (The evaluation of $\mathcal{V}(\epsilon)$ is discussed in Sub-section 2.3.3.2.) The secondary properties f, K_2 and ν, and K_3 are related to the target properties through the curves of Figures 5, 6, and 7, respectively. The kinetic energy fraction, g, is calculated, as discussed previously, from the one-dimensional impact of infinite slabs, one of the target material and one of the penetrator material.

It is useful to compare the present results with those developed for the rigid penetrator, one-dimensional impact at constant shock density. For this purpose, it is sufficient to restrict the comparisons to the zeroeth order terms as the first and higher order terms account for the variation in the flow-field levels with impact velocity. The basic characteristics of the flow process, i.e., the amount of geometric divergence and shock density variation, are reflected in the form of the leading term of the shock position series.

When comparing the one-dimensional and spherical flow analyses, it is instructive to note that for explosive shock flows at constant shock density, the shock front motion varies with flow-field geometry as

$$R \propto t^{2/n} \tag{39}$$

where n =3, 4, and 5 for one-dimensional, cylindrical, and spherical flows, respectively. For one-dimensional flow with a constant shock density, Equation (61) of Part I gives the leading term of the shock position series as

TABLE 1. FIRST ORDER SERIES EXPANSIONS *

Particle Position

$$r(m,t) \approx a\left\{g^{1/4} + \left[\frac{4K_2}{(12-3\beta)}\left(\frac{c}{v_0}\right)^{\frac{\nu-\beta}{\nu\delta}}\left(\frac{12}{12-3\beta}\right)^{-4\gamma}g^{\left(\frac{\beta}{4\delta}-\frac{1}{4}\right)}\left(h^{\frac{\gamma_1-1}{\delta_1}}-1\right)+X_1\right]\epsilon\right\}$$

Shock Position

$$R(t) \approx \beta r_0 + ct - (\beta-1)a + \beta a\left\{X_1 + \left(\frac{v_2}{c}\right)\frac{\delta}{(12-3\beta)}\left[\frac{g^{\ell_1}-1}{\ell_1} - \frac{(g^{\ell_2}-1)}{\ell_2}\right]\right\}\epsilon$$

Modified-Penetrator Position

$$X(t) = a g^{1/4} + a\left\{g^{\omega_R}\left[C_1\cos(\omega_I \ln g) + C_2 \sin(\omega_I \ln g)\right] + \sum_{i=1}^{7} \mathcal{L}_i g^{\ell_i}\right\}\epsilon$$

Pressure

$$P(m,t) \approx \left(\frac{12}{12-3\beta}\right)\rho^0 v_0^2 g^{-9/4} h + \left\{(I_1 - I^*) - (I_2 - I_2^*) + \frac{\rho^0}{\beta}(2\dot{R}_0\dot{R}_1 - c\dot{R}_1)\right\}\epsilon$$

Density

$$\rho(m,t) \approx \rho^0\left(\frac{12}{12-3\beta}\right)^{1/\alpha}\left(\frac{v_0}{c}\right)^{\frac{\nu-\alpha}{\nu\alpha}} g^{-9/4\alpha} G^{\frac{\nu-\beta}{\nu\alpha}} h^{1/\alpha};$$

$$g \equiv 1 + \frac{4v_0 t}{a}, \qquad h \equiv 1 + \frac{(12-3\beta)}{4}\frac{m}{\rho^0 a^3}.$$

Other symbols are defined in the nomenclature.

* The first order density term is not included. It is not required for calculating shock motion and the transient pressure and velocity fields.

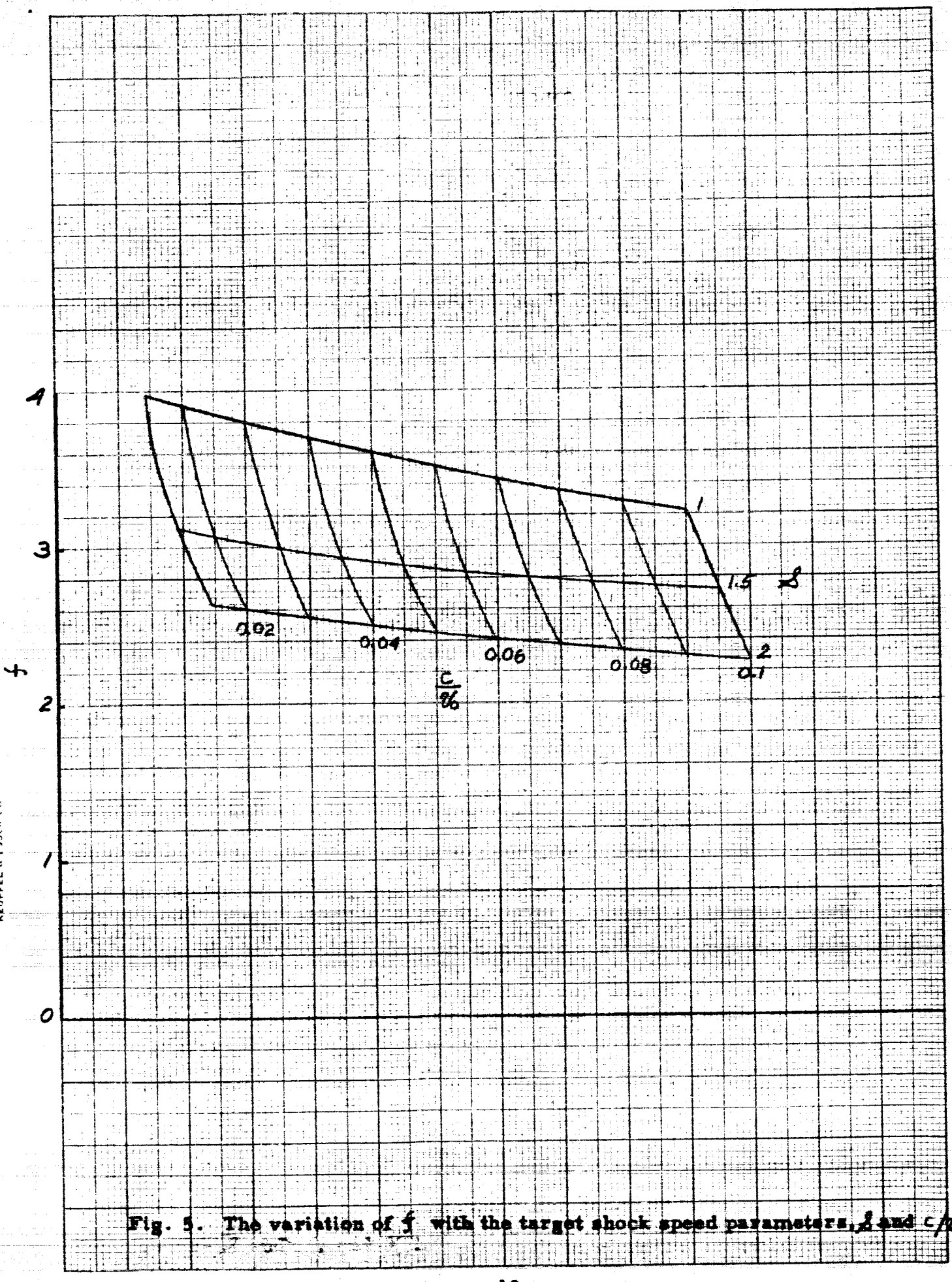

Fig. 5. The variation of f with the target shock speed parameters, M and $C/\%$.

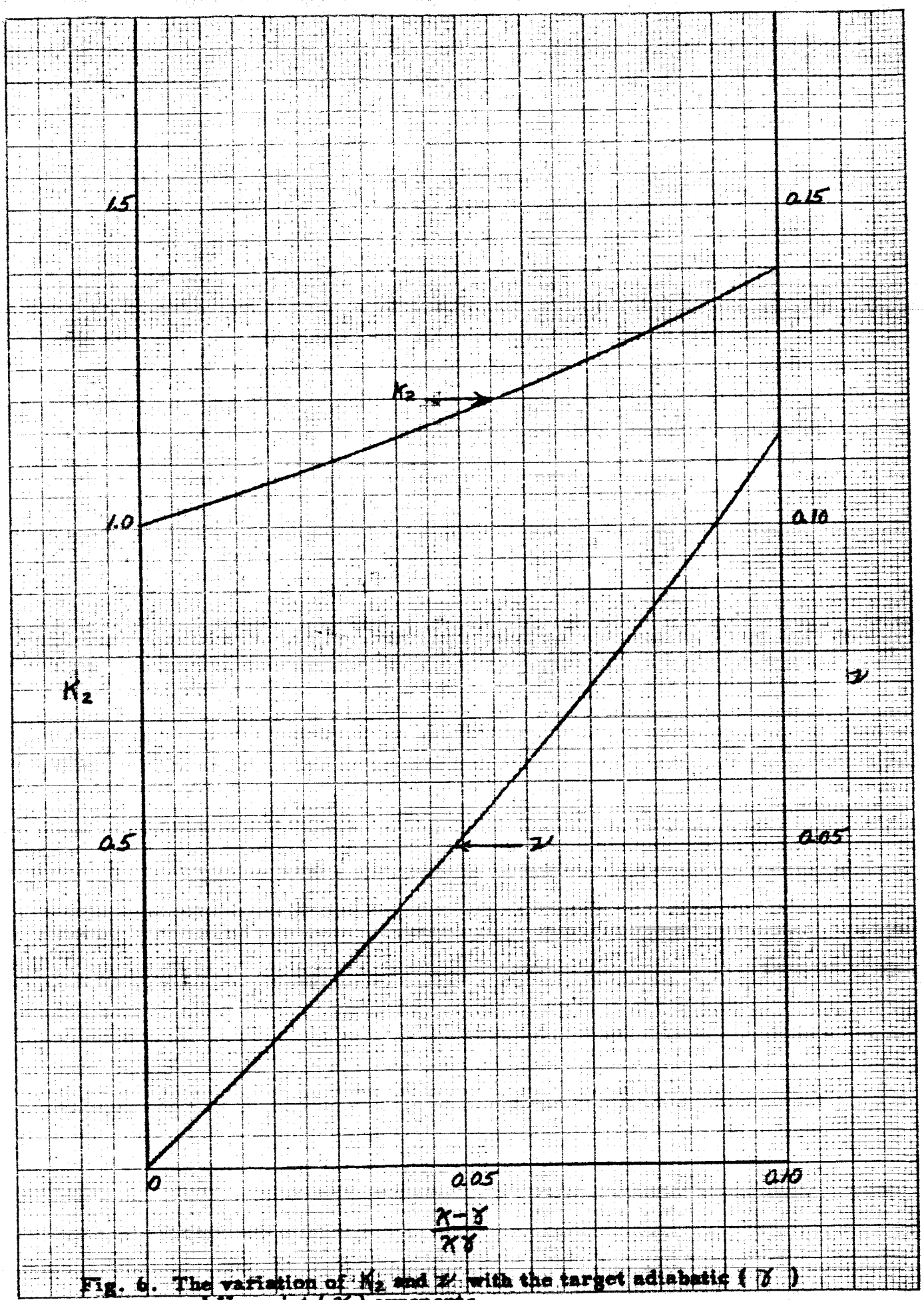

Fig. 6. The variation of K_2 and γ with the target adiabatic (δ) and Hugoniot (γ) exponents.

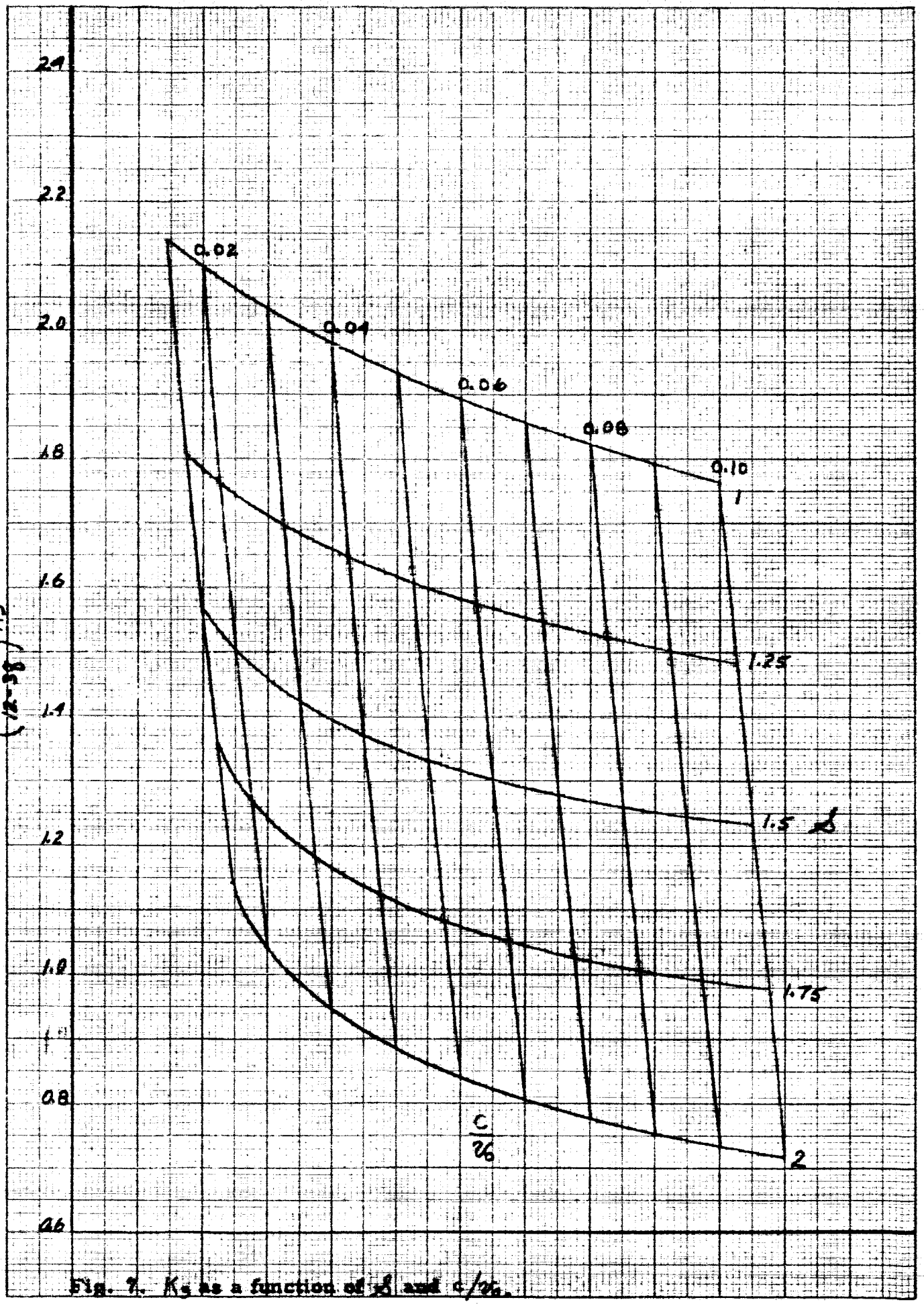

Fig. 7. K_3 as a function of δ and $c/2b$.

$$R_o \propto g^{1/2} \propto t^{1/2} \qquad \text{(one-dimensional, constant shock density)}^{*} \qquad (40)$$

where the reduction of the exponent from 2/3 (as predicted for one-dimensional explosive shock flow) to 1/2 is due to the fact that the Part I analysis allows for a continuous deposition of penetrator energy into the target flow-field as contrasted to the instantaneous deposition postulated for the explosive shock model.

In complete analogy with the reduction of exponent when comparing one-dimensional and spherical explosive shock flows, R_o for the present spherical flow is**

$$R_o = \lambda a g^{1/4} + ct - (\lambda - 1)a \qquad \text{(spherical, variable shock density);} \qquad (41)$$

for early times,

$$R_o \propto g^{1/4} \propto t^{1/4} \qquad \text{(spherical, constant shock density)} \qquad (42)$$

That is, the exponent is reduced from 1/2 for the plane case (Equation (40)) to 1/4 for the corresponding early time spherical case. Since the density is relatively constant during the early part of the impact process, Equation (42) is also the constant shock density spherical flow solution.†

The effect of target shock density variation is given by the second term on the right side of Equation (41). As time increases, this becomes the major contribution to R_o ***; thus, $\dot{R} \rightarrow \dot{R}_o \rightarrow c$, i.e., the shock velocity

* $g_{PLANE} \equiv 1 + \frac{2v_o t}{L}$.

** $g_{SPHERICAL} \equiv 1 + \frac{4v_o t}{a}$.

*** The term $(1 - \lambda)a$ serves to satisfy the initial condition $R_o = a$.

† It should also be noted that for corresponding spherical flows, the exponent of the present analysis is smaller than that corresponding to an explosive shock model, viz., 1/4 compared to 2/5, in complete analogy with the plane case results.

approaches the adiabatic bulk sonic velocity. Hence, the removal of the one-dimensional and constant shock density assumptions results in a shock front equation which predicts sonic speed spherical flow at large times and constant shock density spherical flow for early times.

The first order terms of Table 1 become approximate as $g \to \infty$. These expressions are valid for values of g less than 100. This restriction is necessary to obtain an accurate, closed form expression for R_1 and, hence, the other first order coefficients.*

At the instant of impact the retention of only the zeroeth and first order terms leads to deviations (which increase with ϵ) from the impact values of the flow-field properties. However, the effect of the second and higher order terms decay quite rapidly with time**, thus rendering the two term series quite accurate over the major portion of the g range of physical interest.

2.3.3.2 Impact Particle Velocity-Density Ratio Function

In the impacted target layer, the uniform particle velocity and pressure are given by (see Equations (1) and (2))

$$u^*(0) = (1-\epsilon)\,\dot{R}(0) = V \qquad (43)$$

$$p^*(0) = \rho^0(1-\epsilon)\,\dot{R}^2(0) = P_{IMPACT}, \qquad (44)$$

* The evaluation of R_1 is fully discussed in Section A.4.

** As illustrated by the three term Part I analysis.

so that

$$P^*(0) = P^*_{IMPACT} = \frac{\rho^\circ V^2}{1-\epsilon}. \qquad (45)$$

The target Hugoniot function can be introduced to provide a second relationship between impact pressure (i.e., initial shock pressure) and impact density ratio (i.e., initial shock density), viz.,

$$P^*(0) = P_H(\epsilon) \equiv H(P^*, \rho^*, P^\circ, \rho^\circ). \qquad (46)$$

Eliminating $P^*(0)$ from Equations (45) and (46) yields

$$V(\epsilon) = \sqrt{\frac{(1-\epsilon) P_H(\epsilon)}{\rho^\circ}}. \qquad (47)$$

Physically, an ϵ value of zero is not realizable as it corresponds to an infinite shock density and a corresponding infinite shock pressure and impact particle velocity. However, as discussed in Section 3.3.1 of Part I, we seek series solutions to the differential equations for the range $0 < \epsilon \leq 1$, recognizing that the differential equations and their solutions are not correct physical representations for $\epsilon = 0$. In precisely the same manner, a $V(\epsilon)$ curve is constructed from available Hugoniot data and the resulting curve extrapolated to zero. For $\epsilon > 0$, the generated $V(\epsilon)$ curve is a valid representation of the relationship between impact particle velocity and density ratio. Each target material has its own unique curve which follows directly from its Hugoniot data through the application of Equation (47).

The evaluation of the coefficients of the power series representation of $V(\epsilon)$, i.e.,

$$V(\epsilon) = V_0 + V_1 \epsilon + \cdots, \qquad (48)$$

follows directly from the curve itself. Thus,

$$v_0 = v(0) \qquad (47a)$$

$$v_1 = \left.\frac{dv}{d\epsilon}\right|_{\epsilon=0} \qquad (47b)$$

$$\vdots \qquad \vdots$$

At this point it is well to emphasize that the impact particle velocity, v and the actual penetrator impact velocity V, are related through Equation (5), i.e.,

$$v = \frac{8}{2} V.$$

The factor $8/2$ accounts for the spherical flow-field and the penetrator compressibility.* For a given penetrator impact velocity, V, the impact particle velocity, v, follows from Equation (5); the corresponding impact density ratio, ϵ, is obtained from the $v(\epsilon)$ curve specified by Equation (47).

* In the rigid penetrator, one-dimensional analysis, $v = V$.

3. NUMERICAL CALCULATIONS

The purpose of this section is to illustrate the application of the flow field series equations by calculating the depth of penetration-impact velocity relationship for aluminum-aluminum impacts. The procedure presented is quite general and is not restricted to similar material impacts. The only calculational simplification offered by a similar material impact (within the framework of the present model) is that β, the kinetic energy fraction, is known to be 1/2; hence, the one-dimensional, infinite media impact calculation need not be made.

3.1 Material Properties

The specification of the values of the material properties required for the calculations is described in this section. A summary table is given in Sub-Section 3.1.5.

3.1.1 $V(\epsilon)$ Curve

From Equation (47),

$$V(\epsilon) = \sqrt{\frac{(1-\epsilon)\, P_H(\epsilon)}{\rho^0}} \, .$$

The Hugoniot curve for Aluminum, i.e., $P_H(\epsilon)$, is taken from Reference 4 and is shown in Figure 8. Hence,

$$V \text{ ft/sec} = \left(\frac{(1-\epsilon)(P_H \text{ Mb})(2.09 \times 10^9 \text{ lb}^2/\text{ft}^4\text{-Mb})}{5.23 \text{ slug/ft}^3} \right)^{1/2}$$

or

$$V(\epsilon) = 20{,}000 \sqrt{(1-\epsilon)\, P_H(\epsilon)} \, .$$

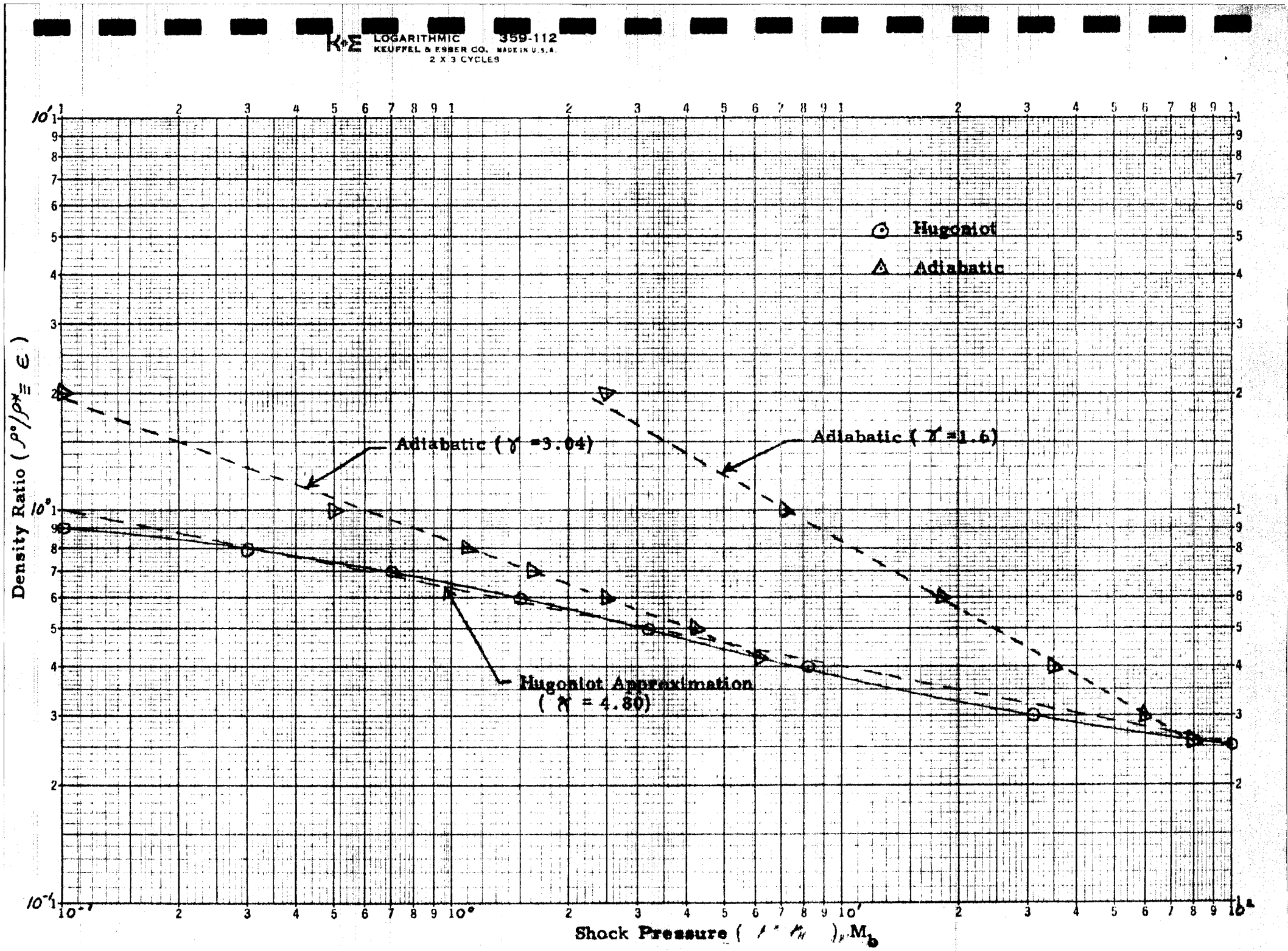

Fig. 8. The Hugoniot curve and shock release adiabatics for aluminum.

This expression is presented in Figure 9. The upper limit impact velocity of physical interest is taken to be 200,000 ft/sec. Since $\mathcal{V} = V/4$ for similar material impacts, the corresponding upper limit impact particle velocity, $\mathcal{V}$, is 50,000 ft/sec. A smooth curve through the calculated values of $\mathcal{V}$ up to 50,000 ft/sec is extrapolated to $\epsilon = 0$ to give

$$\mathcal{V}_0 = 200{,}000 \text{ ft/sec.}$$

The extrapolated portion of the curve is shown dotted in Figure 9.

The value of $\mathcal{V}_1$ is obtained directly from the curve as (see Equation 49b)

$$\mathcal{V}_1 = \left.\frac{d\mathcal{V}}{d\epsilon}\right|_{\epsilon=0} = -690{,}000 \text{ ft/sec},$$

so that

$$\frac{\mathcal{V}_1}{\mathcal{V}_0} = -3.44.$$

3.1.2 κ and γ

As can be seen in Figure 8, the Hugoniot curve can be well represented by

$$p^* \epsilon^{\kappa} = \text{CONSTANT}$$

or

$$p^* \rho^{*-\kappa} = \text{CONSTANT}$$

for ϵ values greater than 0.37 (corresponding to $\mathcal{V} > 50{,}000$ ft/sec). The Hugoniot exponent, κ, is given by

$$\kappa = 4.3.$$

The adiabatic exponent, γ, varies significantly more than κ with ϵ Reference to Figure 8 shows the change of γ with initial state. Thus, for

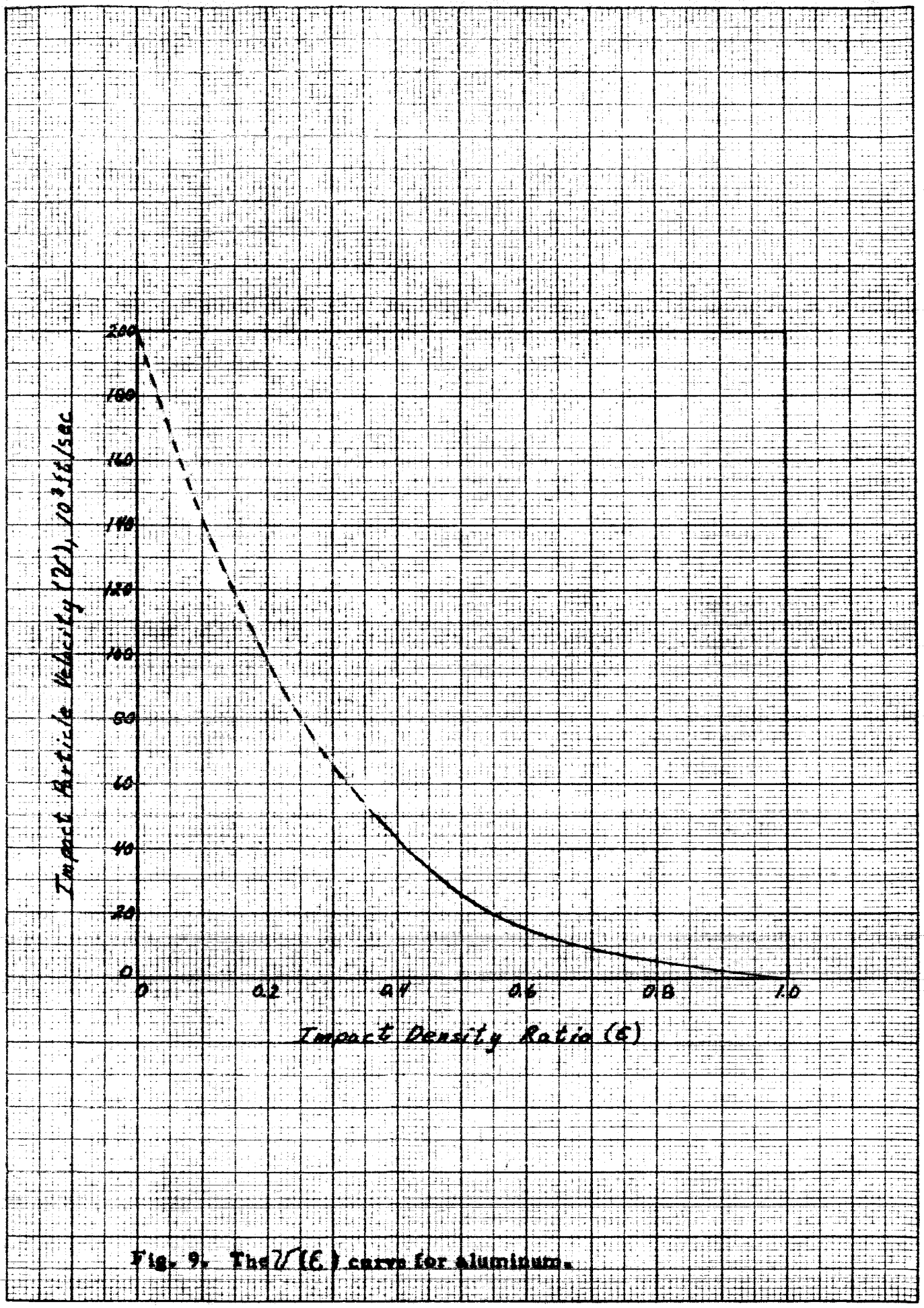

Fig. 9. The $V(\varepsilon)$ curve for aluminum.

initial pressures greater than 40 megabars, the compressed target expands adiabatically from its initial shocked state as if it were a gas. That is γ is about 1.6. It is an interesting fact that only when the initial shock pressure is considerably smaller, e.g., levels of about 1 megabar or less, does the adiabatic exponent approach the larger values normally associated with metallic state adiabatic expansion, say 5 or 6, or thereabouts.

For the purposes of the present calculation, an average value of γ is utilized. At an $\epsilon = 0.37$ (corresponding to $\mathcal{V}$ =50,000 ft/sec), the initial shock pressure is 10 megabars. The corresponding value of γ is 3.07 (see Figure 8). For $\mathcal{V}$ =10,000 ft/sec, the initial shock pressure is about 1 megabar and the corresponding value of γ is 6.[6] Hence the average value of γ over the range of impact particle velocities is

$$\gamma = (3.07 + 6)/2$$

$$\gamma = 4.53.*$$

3.1.3 ℓ and C

From Reference 7, the appropriate values of ℓ and C for aluminum are

$$\ell = 1.37$$
$$C = 17{,}400 \text{ ft/sec}.$$

3.1.4 Secondary Properties: f, v, K_2, K_3, and γ_1

From Figure 5, for $C/\mathcal{V}_s$ =17,400/200,000 = 0.087, and ℓ = 1.37,

$$f = 2.9.$$

*It should be noted that the analysis is carried out under the assumption that γ is constant. The results of the plane case study indicate that indeed the shock motion is relatively insensitive to values of γ. However, for slightly increased accuracy, the value of γ can be allowed to vary with ϵ in making the numerical flow-field calculations.

From Figure 6, for $(\kappa-\gamma)/\kappa\gamma = (0.27)/(4.8)(4.53) = 0.0124$,

$$\mathcal{V} = 0.012$$

$$K_2 = 1.04$$

Lastly, from Figure 7, $4K_3/(12-3\beta) = 1.30$, so that, since $\beta = 0.5$,

$$K_3 = 3.56.$$

From Equation (A43),

$$\frac{1}{\gamma_1} = \frac{1}{c} + \mathcal{V} = \frac{1}{4.53} + 0.012,$$

or

$$\gamma_1 = 4.28.$$

3.1.5 Summary of Material Property Data

The values of the material properties necessary for calculating Al-Al impacts are given in Table 2.

TABLE 2 - MATERIAL PROPERTY DATA FOR ALUMINUM-ALUMINUM IMPACTS

Primary Properties		Secondary Properties	
β	= 0.5	f	= 2.9
ρ°	= 5.23 slug/ft^3	$\mathcal{V}$	= 0.012
V_0	= 200,000 ft/sec	K_2	= 1.04
V_1	= -089,000 ft/sec	K_3	= 3.56
γ	= 4.53	γ_1	= 4.28
κ	= 4.80		
δ	= 1.37		
c	= 17,400 ft/sec		

3.2 Solution Constants

Using the data of Table 2, the solution constants given by Equations (A57) through (A63) are readily calculated. The numerical values are summarized in Table 3.

TABLE 3 - SOLUTION CONSTANTS FOR ALUMINUM-ALUMINUM IMPACTS

$\mathcal{L}_1 = -0.114$	$l_1 = 0.79$	$\omega_K = 0.055$
$\mathcal{L}_2 = 0.49$	$l_2 = -0.004$	$\omega_I = 0.61$
$\mathcal{L}_3 = 5.8\times10^{-5}$	$l_3 = 1.26$	
$\mathcal{L}_4 = -6.88\times10^{-3}$	$l_4 = 0.28$	$C_1 = -0.323$
$\mathcal{L}_5 = 0.0515$	$l_5 = -1.03$	$C_2 = -1.34$
$\mathcal{L}_6 = -1.96\times10^{-4}$	$l_6 = 0.47$	
$\mathcal{L}_7 = 5.76\times10^{-3}$	$l_7 = 0.51$	$\frac{\nu_2}{c}\left(\frac{\xi}{12-9\xi}\right) = -0.00186$

3.3 Depth of Penetration - Impact Velocity Relationship

In order to evaluate depth of penetration, a cratering-cessation criterion is required. In accordance with the discussion of Section 4.3 of Part I, the crater depth is defined as the position of the shock front (defined as R_c) at the instant the the shock pressure falls below σ^*, the dynamic yield stress. Hence, R_c is calculated as follows:

1. For a given impact velocity, V, and corresponding ϵ, $R = R_1 + R_2 \epsilon$ and $\dot{R} = \dot{R}_1 + \dot{R}_2 \epsilon$, the transient shock position and velocity histories, respectively, are calculated.*

2. From Equation (20), the velocity (defined as $\dot{R}_c$) corresponding to σ^* is

*The generalized time, $q \equiv 1 + \frac{4Vt}{a}$ is used as the time variable for convenience.

calculated.

3. The time (defined as g_c)corresponding to $\dot{R}_c$ is obtained from the transient shock velocity history calculated in Step 1.

4. The shock radius at the time g_c , which is by definition the depth of penetration according to the stated cratering-cessation criterion, follows directly from the transient shock position history of Step 1.

5. This sequency of steps is repeated for several values of ϵ to determine the general relationship between depth of penetration and impact velocity.

3.3.1 Transient Shock Position and Velocity Histories

Using the solution constants of Table 2, R_1/a is calculated as a function of g by means of Equations (A64) and (A56). The leading term of the shock series, R_0/a, follows directly from Equation (A31). The resultant shock front motion for any ϵ is simply

$$\frac{R}{a} \approx \frac{R_0}{a} + \frac{R_1}{a}\epsilon .$$

Figure 10 shows R(g) for ϵ values of 0.0, 0.35, 0.4, 0.45, & 0.6.*

The corresponding shock velocity, obtained by differentiating Equations (A31) and (A64) and noting that

$$\frac{dR}{dt} \equiv \dot{R} = \frac{dR}{dg}\frac{dg}{dt} = \frac{dR}{dg}\frac{4V_0}{a}, \qquad (51)$$

*The corresponding impact particle velocities, V , follow directly from Figure 9. The impact velocities, V, are just 4 times these values. Thus,

ϵ	V	V
0.35	54,000	216,000
0.40	43,000	172,000
0.45	34,000	136,000
0.60	15,000	60,000

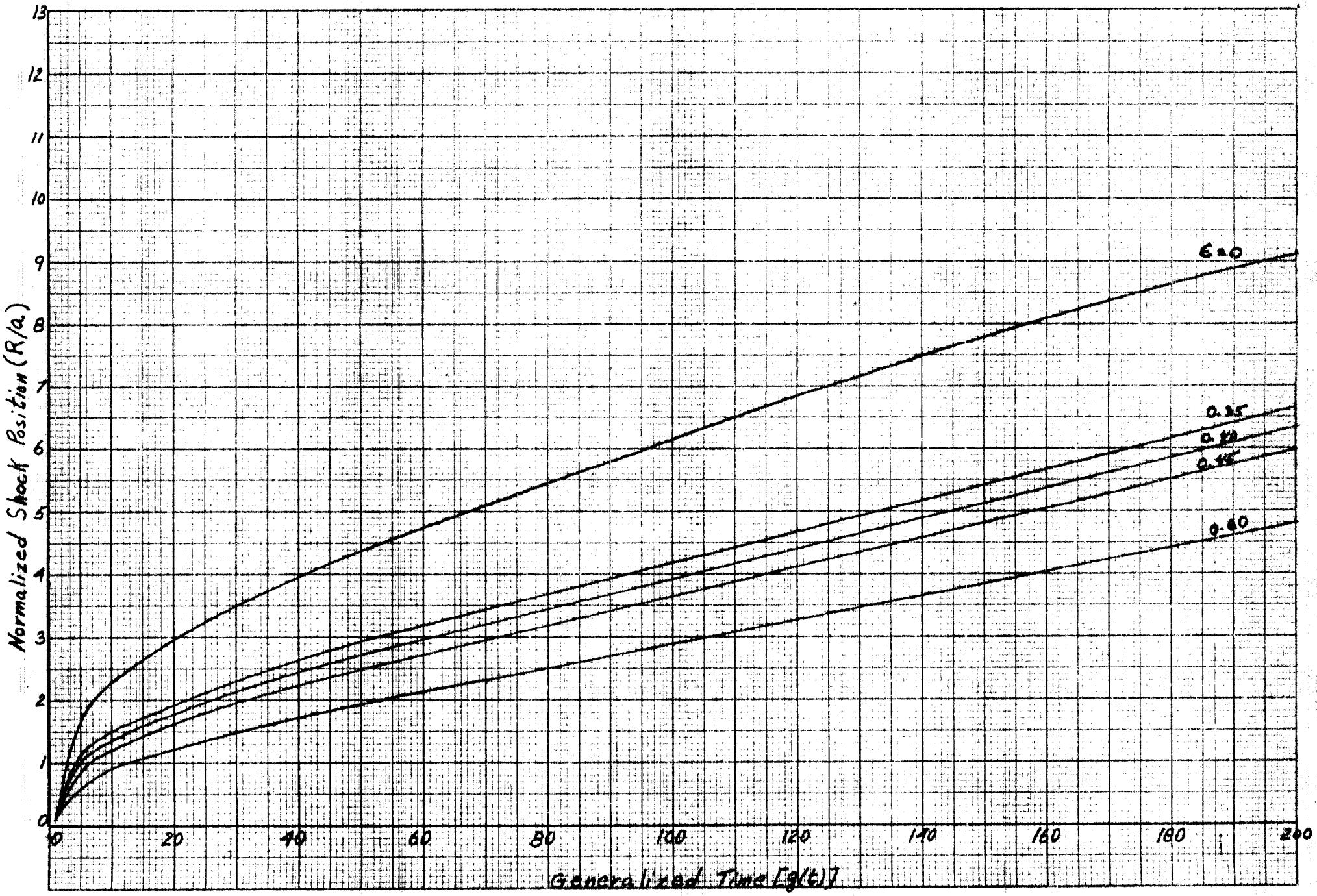

Fig. 10. Transient shock front position for various aluminum-aluminum impacts.

is shown in Figure 11 for the various values of ϵ . It should be remarked that for values of g less than 10, the two term approximation for $\dot{R}$ deteriorates for the ϵ values chosen. That is, more than 2 terms are necessary to accurately describe the early time behavior. Fortunately, however, the effect of the higher order terms dies out rapidly* and it is possible to draw a smooth curve though the values of $\dot{R}$ for g > 10 to the true impact shock velocity obtained from Equation (19). For g values close to 100, the analytical approximations used in deriving R_1 in closed form break down. Hence for values of g greater than 50, the $\dot{R}$ curves are extrapolated rather than calculated. As mentioned previously, and as will be shown, the cratering process is terminated before g reaches 100, so that this small extrapolation introduces no uncertainty into the calculation.

3.3.2 Calculating P/D

Figure 12 illustrates Equation (20) in the low pressure and velocity range. To be specific, consider the case where the dynamic yield stress is 0.01 Mb. The corresponding shock velocity is 17,700 ft/sec. From Figures11 and 10, the corresponding cratering times and shock radii are as given in Table 4.

Lastly, since depth of penetration data are normally presented as P/D, where P is the crater radius and D is the equivalent spherical diameter of the penetrator, Equation(7b) is used to relate a to D of the penetrator. Thus,

$$m_p = \frac{\pi}{6} \rho_p^\circ D^3 \qquad (52)$$

so that

$$a = \left(\frac{3 m_p}{2\pi \rho^\circ} \left[\frac{4}{\beta} - 1 \right] \right)^{1/3},$$

or for $\rho^\circ = \rho_p^\circ$ and $\beta = 0.5$,

$$a = 1.2\, D.$$

* Based on the results of the one-dimensional analysis.

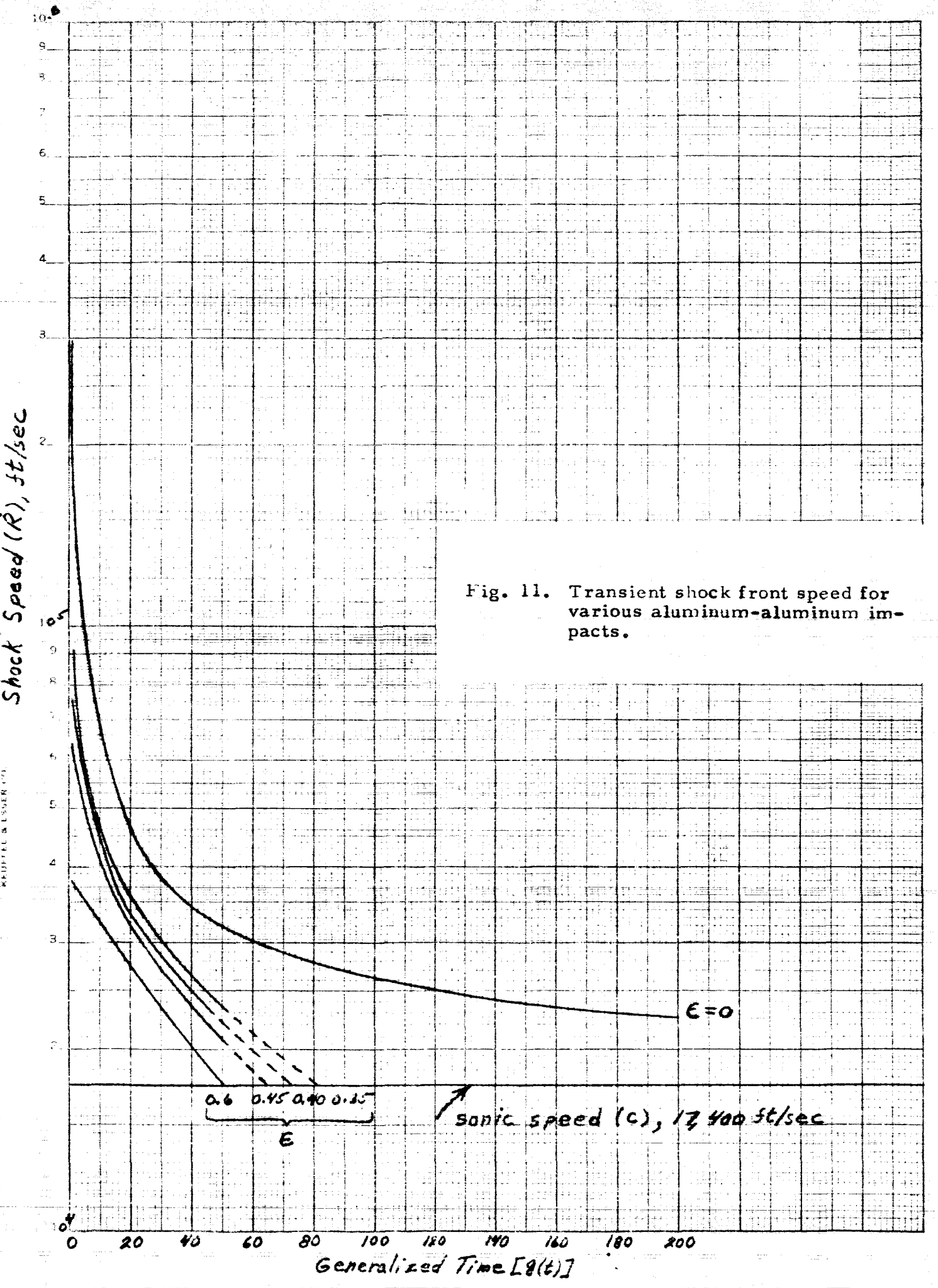

Fig. 11. Transient shock front speed for various aluminum-aluminum impacts.

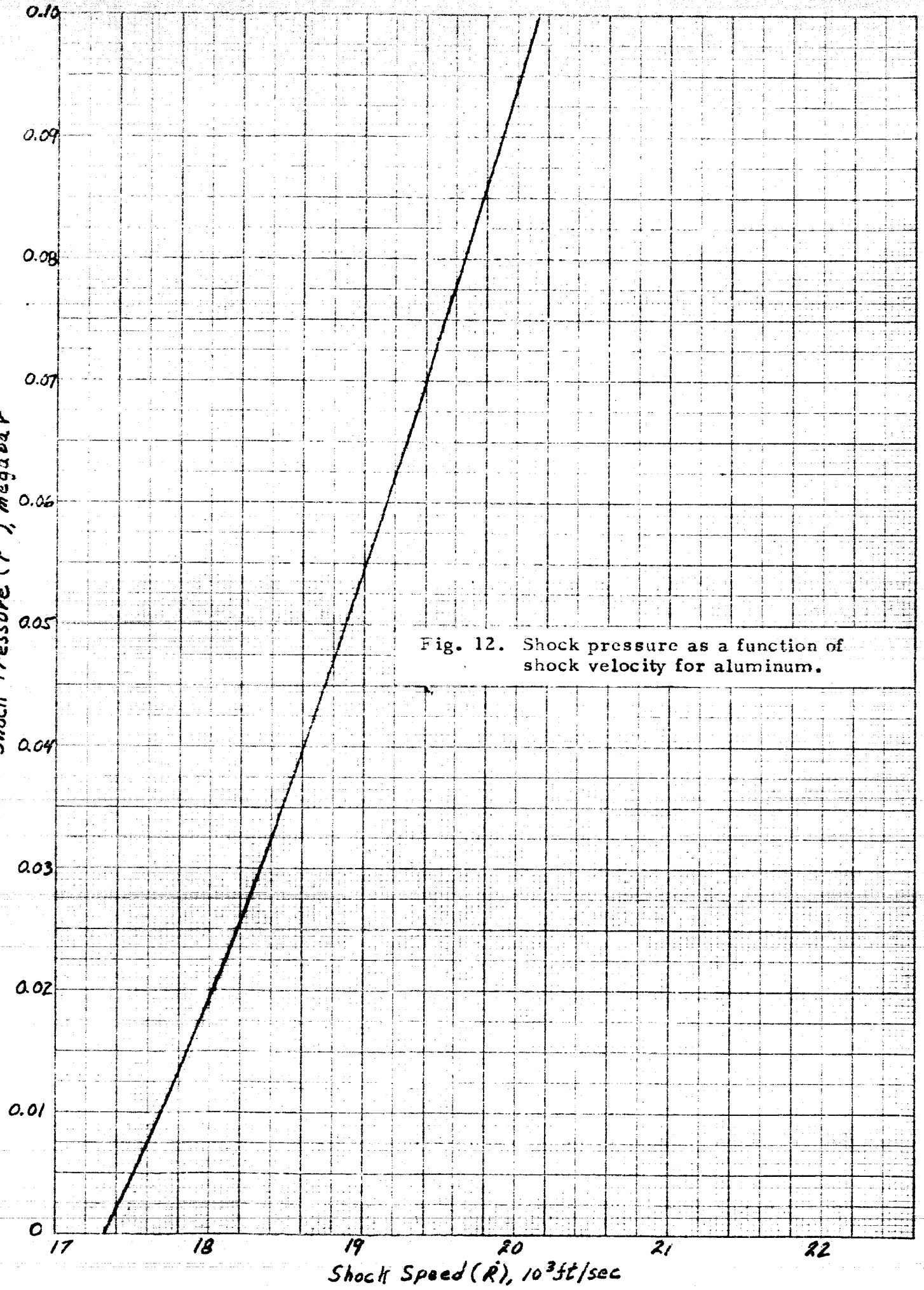

Fig. 12. Shock pressure as a function of shock velocity for aluminum.

Hence,

$$\frac{P}{D} \equiv \frac{R_c}{D} = \frac{R_c}{a/1.2} = 1.2\,\frac{R_c}{a}. \qquad (53)$$

These values are also given in Table 4.

TABLE 4 - NORMALIZED DEPTH OF PENETRATION FOR VARIOUS IMPACT VELOCITIES ($\sigma^* = 0.01$ Mb)

ϵ	V	ϑ_c	R_c/ϑ	P/D
0.35	216,000	71	3.45	4.14
0.40	172,000	66	3.10	3.72
0.45	136,000	61	2.70	3.24
0.60	60,000	49	1.80	2.16

Figure 13 shows the relationship between P/D and V for σ^* values of 0.01 and 0.1 Mb. As expected, the higher yield stress yields the lower depth of pentration. However, a 10-fold change in σ^*, does not affect a corresponding large change in depth of penetration. This follows from the shock velocity-pressure relationship; that is, at low pressure levels, a small change in $\dot{R}$ gives rise to a large relative change in pressure level. Hence, even though the relative change in pressure may be large, the corresponding velocity (and hence ϑ_c and R_c) difference is quite small.

The data of Figure 13 follow a power law relationship

$$\frac{P}{D} \propto V^{\alpha}$$

where $\alpha = 0.56 \pm 0.03$. This agrees very closely with the 0.58 value quoted by Walsh based on his extensive machine computations.

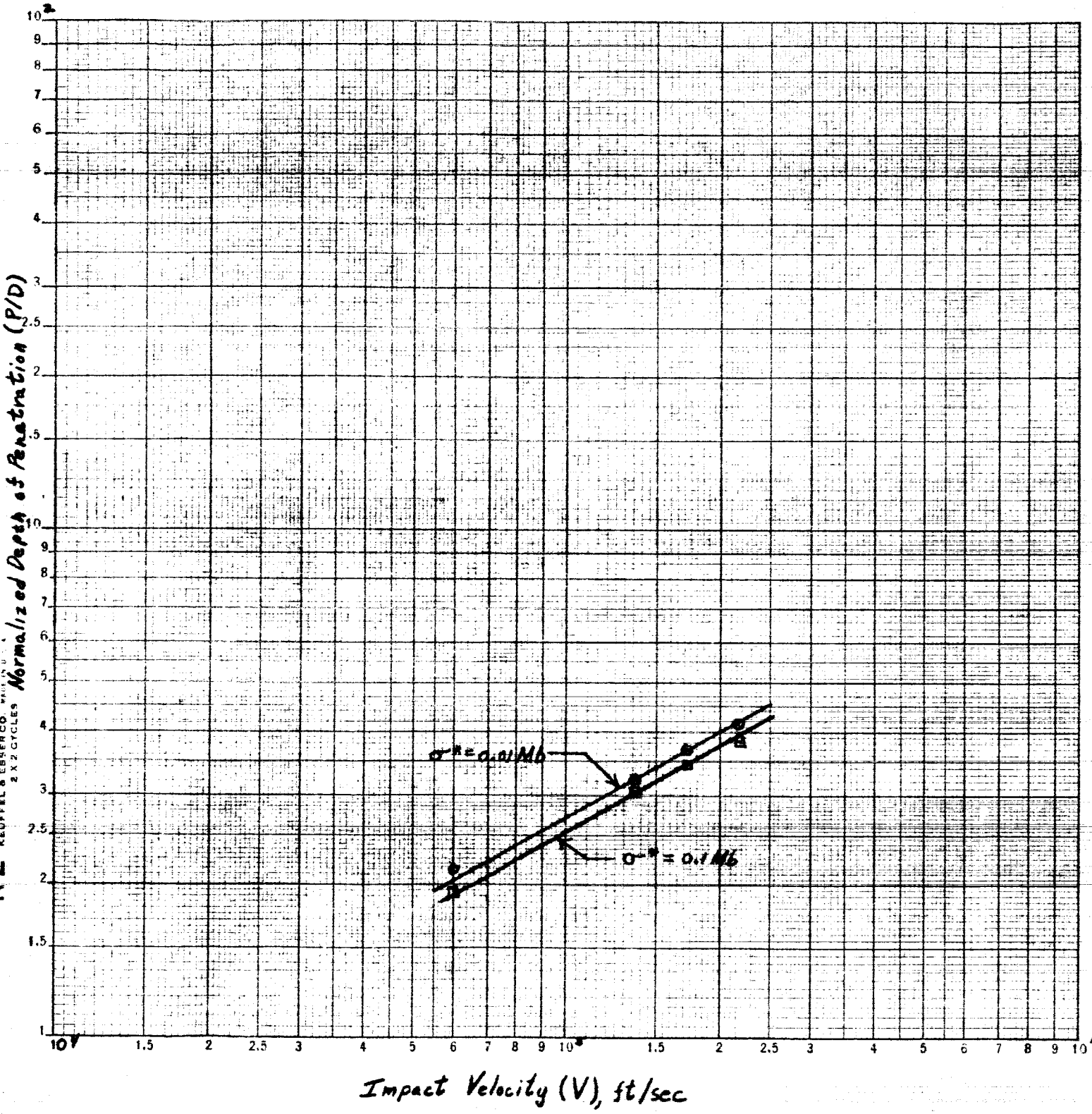

Fig. 13. The depth of penetration-impact velocity relationship for aluminum-aluminum impacts. The slope of the curves, which is the velocity exponent, α, is 0.56 ± 0.03.

4. CONCLUSIONS

1. The series solution technique provides a useful means for describing the hydrodynamic phase flow-field during a hypervelocity impact without the necessity of extensive computer codes and calculations.

2. Using simple Hugoniot data to provide the necessary material property data, it is possible to easily calculate the target's spherical flow-field while accounting for

   a. continuous energy deposition

   b. variable shock density

   c. penetrator compressibility.

3. Based on the calculation presented and its specific cratering-cessation criterion, the penetration-velocity exponent is 0.56 ± 0.03. It appears that simple penetrator energy scaling ($\alpha = 2/3$) or momentum scaling ($\alpha = 1/3$) is not appropriate and that both quantities affect the crater size (of course, along with target strength and other properties, i.e., Y, K, λ, C, and ρ°).

REFERENCES

1. Walsh, J.M. and Johnson, W.E. On the Theory of Hypervelocity Impact. Proceedings of the Seventh Hypervelocity Impact Symposium, Vol. II, p.48. Tampa. 1964.

2. Olshaker, A.E. and Bjork, R.L. Hydrodynamics Applied to Hypervelocity Impact I. Scaling Laws for Dissimilar Materials. Proceedings of the Fifth Symposium on Hypervelocity Impact, Vol. I, Pt. 1, p. 191. Denver, 1961.

3. Courant, R. and Friedrichs, K.O. Supersonic Flow and Shock Waves, p.32. New York, Interscience Publishers. 1948.

4. Walsh, J.M. and Tillotson, J.H. Hydrodynamics of Hypervelocity Impact. Proceedings of the Sixth Symposium on Hypervelocity Impact, Vol. II, Pt. 1, p. 68. Cleveland. 1963.

5. Tillotson, J.H. Metallic Equations of State for Hypervelocity Impact. Company Report, General Atomic, GA-3216, July, 1962.

6. Davids, N. et al. Spherical Shock Waves and Cavity Formation in Metals. Proceedings of the Sixth Symposium on Hypervelocity Impact, Vol. II, Pt. 1, p. 247. Cleveland. 1963.

7. Gault, D.E. and Heitowit, E.D. The Partition of Energy for Hypervelocity Impact Craters Formed in Rock. Proceedings of the Sixth Symposium on Hypervelocity Impact, Vol. II, Pt. 2, p. 426. Cleveland. 1963.

8. Rice, M.H. et al. Compression of Solids by Strong Shock Waves. Solid State Physics, Advances in Research and Applications, Vol. 6. New York, Academic Press. 1958.

9. Marnell, P., Soiffer, M., and Zaid, M. Hypervelocity Impact - A Series Solution, Part I - One-Dimensional Flow. Proceedings of the Seventh Symposium on Hypervelocity Impact, Vol. III, p. 151. Tampa. 1964.

APPENDIX

The derivation of the zeroeth and first-order series coefficient is presented herein.

A.1 Evaluation of $r_0(t)$

A strongly non-linear second-order differential equation for r_0 is obtained by solving three equations relating $p_0(0,t)$, R_0, and r_0. A simple analytical solution for r_0 is not possible and a useful approximation is obtained based on a numerical solution of the differential equation.

From Equation (32) evaluated at the shock front, i.e., $m = m^*$,

$$p_0(0,t) = p_0(m^*,t) + \frac{\ddot{r}_0}{r_0^2}\, m^*. \tag{A1}$$

In complete analogy with the one-dimensional analysis, it is convenient to consider m^* as $\epsilon \to 0$. Then, from Equation (10),

$$\lim_{\epsilon\to 0} m^* = \lim_{\epsilon\to 0} \frac{\rho^0}{3}\left[R^3 - a^3\right]$$

$$= \lim_{\epsilon\to 0} \frac{\rho^0}{3}\left[(R_0 + R_1\epsilon + \cdots)^3 - a^3\right] \tag{A2}$$

$$= \frac{\rho^0}{3}\left(R_0^3 - a^3\right). \tag{A3}$$

The pressure shock condition, Equation (20), yields

$$\lim_{\epsilon\to 0} p^* = \lim_{\epsilon\to 0} \frac{\rho^0}{g}\left(\dot{R}^2 - c\dot{R}\right)$$

$$\lim_{\epsilon\to 0}\left(p_0^* + p_1^*\epsilon + \cdots\right) = \lim_{\epsilon\to 0} \frac{\rho^0}{g}\left[(R_0 + R_1\epsilon + \cdots)^2 - c\,(R_0 + R_1\epsilon + \cdots)\right], \tag{A4}$$

or

$$\lim_{\epsilon\to 0} p_0^* \equiv \lim_{\epsilon\to 0} p_0(m^*,t) = \frac{\rho^0}{g}\left(\dot{R}_0^2 - c\dot{R}_0\right). \tag{A5}$$

Hence,

$$p_0(0,t) = \frac{\rho^0}{g}\left(\dot{R}_0^2 - c\dot{R}_0\right) + \frac{\ddot{r}_0}{r_0^2}\left[\frac{\rho^0}{3}\left(R_0^3 - a^3\right)\right]. \tag{A6}$$

Two additional equations between r_0, R_0, and $p_0(0,t)$ are obtained from the target-modified-penetrator interface and shock velocity conditions. Thus, from Equation (18),

$$\left.\frac{\partial^2 r}{\partial t^2}\right|_{0,t} = -\frac{2\pi}{M_P} r^2(0,t)\, p(0,t)$$

$$\ddot{r}_0 + \left.\frac{\partial^2 r_1}{\partial t^2}\right|_{0,t}\epsilon + \cdots = -\frac{2\pi}{M_P}\left(r_0 + r_1(0,t)\epsilon + \cdots\right)^2\left(p_0(0,t) + p_1(0,t)\epsilon + \cdots\right), \tag{A7}$$

so that, equating coefficients of like powers of ϵ,

$$\ddot{r}_0 = -\frac{2\pi}{M_P} r_0^2\, p_0(0,t)$$

or

$$p_0(0,t) = -\frac{M_P}{2\pi}\frac{\ddot{r}_0}{r_0^2}. \tag{A8}$$

The shock velocity condition, Equation (19), requires that

$$u^* = \frac{\dot{R} - c}{g}$$

or, since $u^* \equiv \left.\frac{\partial r}{\partial t}\right|_{m^*,t}$,

$$\dot{r}_0 + \left.\frac{\partial r_1}{\partial t}\right|_{m^*,t}\epsilon + \cdots = \frac{\left(\dot{R}_0 + \dot{R}_1\epsilon + \cdots\right) - c}{g}. \tag{A9}$$

Since Equation (A9) must be true for all values of ϵ, it follows that

$$\dot{r}_0 = \frac{\dot{R}_0 - c}{g}, \tag{A10}$$

and, applying the initial conditions implied by Equation (14), i.e.,

$$r_0(0) = R_0(0) = X_0(0) = a,$$

$$r_o = \frac{1}{\delta}\left[R_o - ct + (\delta - 1)a\right] \tag{A11a}$$

$$R_o = \delta r_o + ct - (\delta - 1)a. \tag{A11b}$$

Equations (A6) and (A8) lead to a second differential equation in r_o and R_o, viz.,

$$\frac{\ddot{r}_o}{r_o^2}\left[\frac{\rho^o}{3}(R_o^3 - a^3) + \frac{M_p}{2\pi}\right] + \frac{\rho^o}{\delta}(\dot{R}_o^2 - c\dot{R}_o) = 0. \tag{A12}$$

Substitution of either Equation (A11a) or (A11b) into the preceding expression leads to a non-linear, second-order differential equation in either R_o or r_o. In both cases the resulting differential equation is mathematically formidable and does not readily yield an analytical solution. An analytical approximation for r_o is obtained from a tedious numerical solution of the exact, highly non-linear differential equation

$$\frac{\ddot{r}_o}{r_o^2}\left[\frac{\rho^o}{3}\left\{\delta r_o + ct - (\delta - 1)a\right\}^3 - a^3\right) + \frac{M_p}{2\pi}\right] + \rho^o(\delta \dot{r}_o^2 + c\dot{r}_o) = 0. \tag{A13}$$

Figure A1 illustrates the numerical solution (δ =1.25, c =20,000 ft/sec, c/v_o =0.04, and a =0.01 ft) and the analytical approximation

$$\boxed{\frac{r_o}{a} = \left(1 + \frac{4v_o t}{a}\right)^{1/4} \equiv g^{1/4}.} \tag{A14}$$

Equation (A14) is precisely that which would result if the shock density is assumed constant. That is, if the shock expressions given by Equations (19) and (20) are replaced by

$$u^* = (1 - \epsilon)\dot{R} \tag{A15}$$

$$p^* = \rho^o(1 - \epsilon)\dot{R}^2, \tag{A16}$$

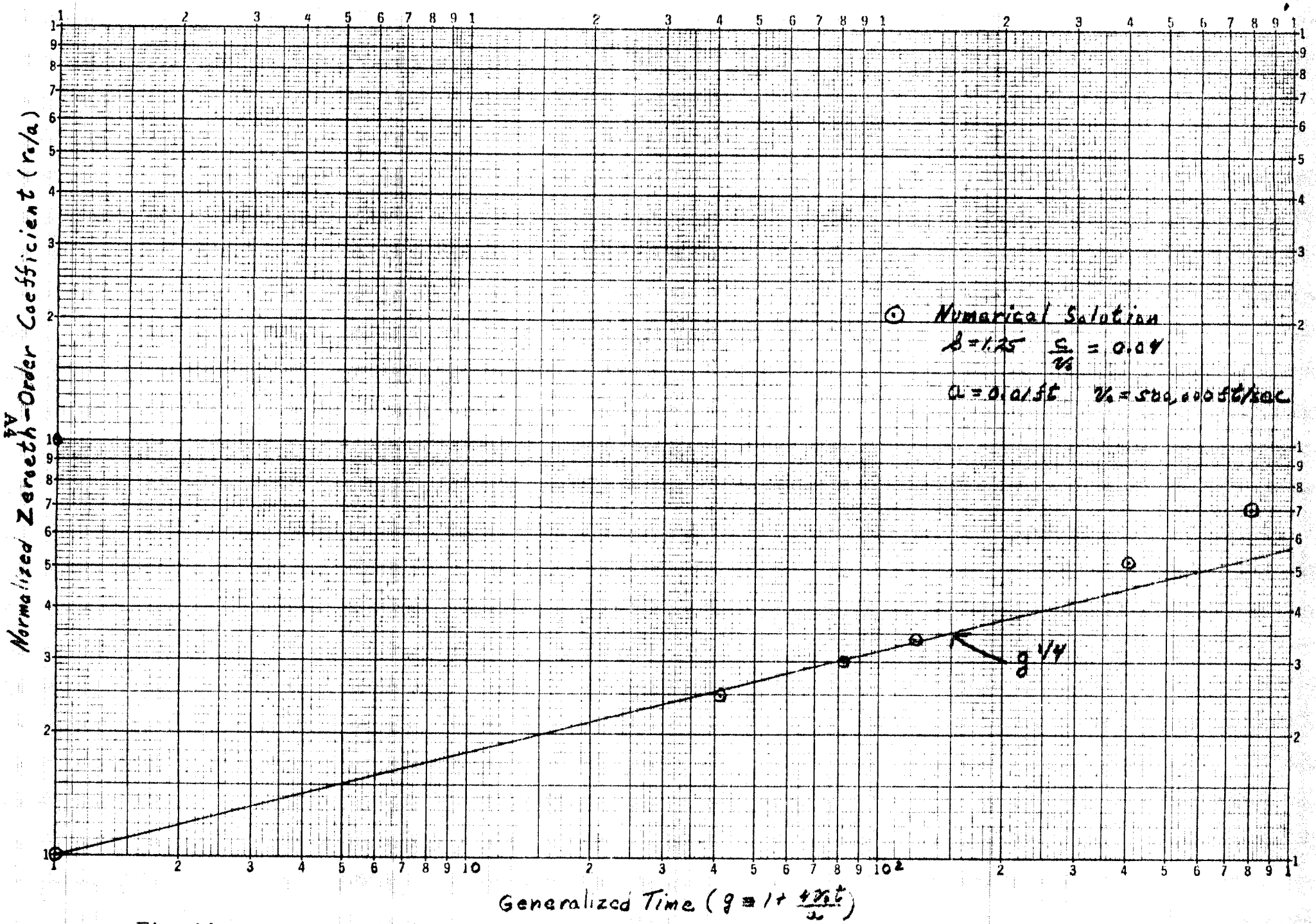

Fig. A1. Comparison of the numerical solution for r_n and the analytical approximation.

the shock conditions utilized in the Part I analysis, the differential equation for r_o is given by

$$\ddot{r}_o = -\frac{3\dot{r}_o^2}{r_o}. \qquad (A17)$$

The solution, subject to the initial conditions

$$r_o = a$$

$$\dot{r}_o = v_o$$

is

$$\frac{r_o}{a} = \left(1 + \frac{4v_o}{a}t\right)^{1/4}.$$

Equation (A13) reduces to (A17) when $\beta = 1$ and $C = 0$*

The approximation given by Equation (A14) does not reflect the effect of the target material properties β and C on r_o. However, analogous calculations for the one-dimensional case with a compressible penetrator and a variable shock density yield an analytical solution for x_o, the leading term of the particle position series, which can be used to ascertain the significance of β and C/v_o. It is found that x_o/L** is relatively insensitive to variations in these parameters (see Figure A2). Furthermore, the case where $\beta = 1.25$ and $C/v_o = 0.04$ lies approximately in the middle of the spread due to the large variations in β and C/v_o.

For the spherical flow case, the difference between r_o/a for $\beta = 1.25$ and $C/v_o = 0.04$

* In both derivations, the term $\left(\frac{M_p}{2\pi} - \frac{\rho_o a^3}{3}\right)$ is neglected relative to $\rho_o r_o^3/3$.

** In the one-dimensional rigid penetrator analysis, L is defined as $m_p/A\rho_o$ (see part I). When the penetrator is considered compressible, $L \equiv M_p/A\rho_o$, where $M_p \equiv m_p/g$.

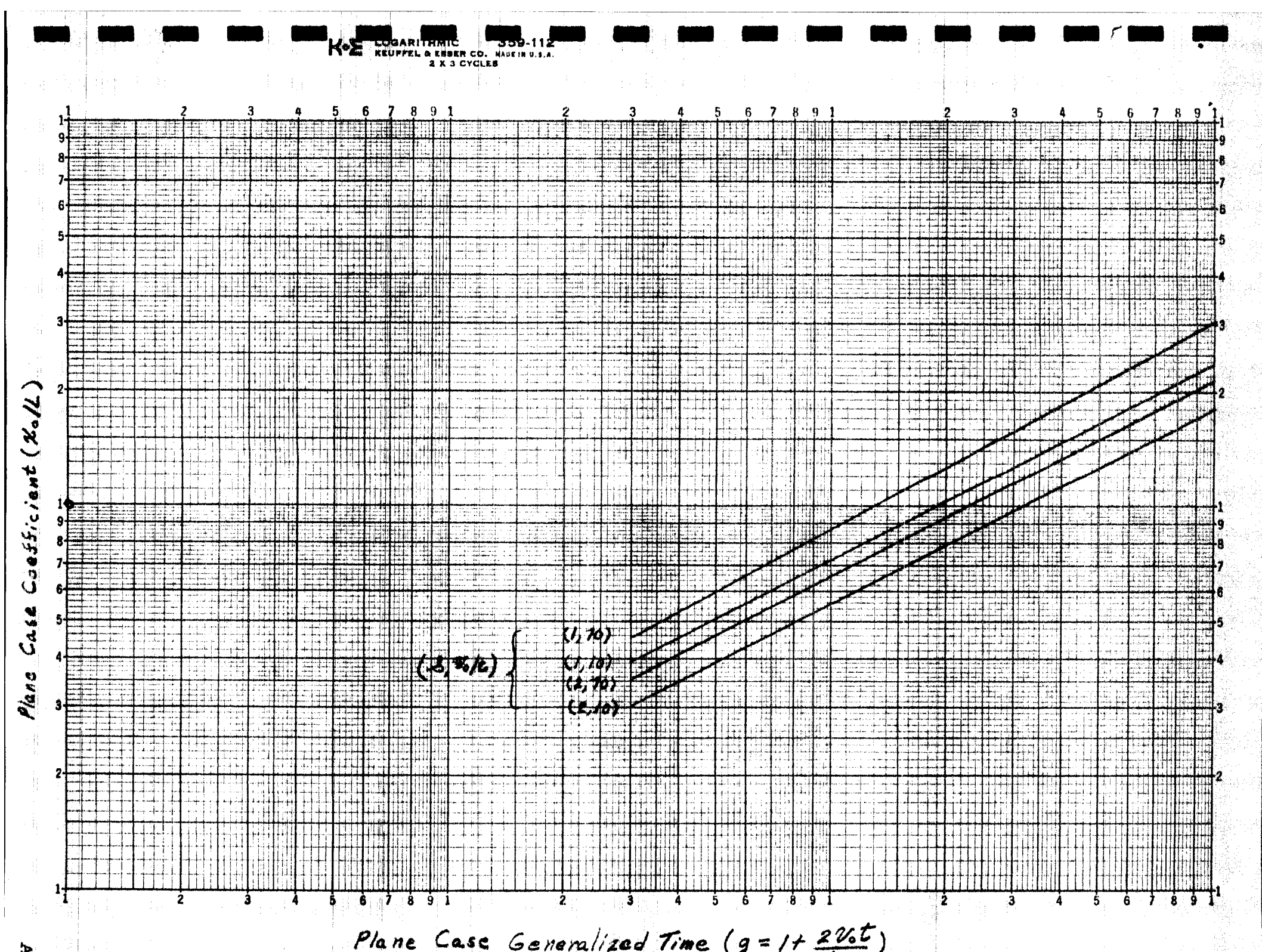

Fig. A2. The effect of β and γ_0/c on the leading coefficient of the one-dimensional particle position series.

and r_0/a for $\lambda = 1$ and $c/v_0 = 0$ (this corresponds to the constant shock density case) is smaller than the corresponding difference for the one-dimensional case so that the overall spread due to the λ, c/v_0 variation is also smaller in the spherical case. Hence, based on the one-dimensional calculations which illustrate the relatively small effect of λ and c/v_0 on x_s/L and the even smaller spread for the spherical case, the expression for r_0 given by Equation (A14) is assumed valid in spherical flow over the range in λ and c/v_0 of practical interest, i.e., $(\lambda, c/v_0)$ varies between (1, 0.015) and (2, 0.10).* It should be emphasized that even though the expression for r_0 does not contain λ and C, the shock term, R_0, given by Equation (A11b) varies markedly with these parameters.

Higher order accuracy in the r_0 approximation can be obtained at the expense of analytical simplicity. However, based on the previous one-dimensional analysis and this part of the spherical development, it is apparent that a less simple representation for r_0 would lead to mathematical complications which would restrict an analytical development through the first order series terms. Thus, Equation (A14) represents a compromise between analytical exactness and complexity which adequately depicts the leading term of the particle position series over the times of physical interest, i.e., $g \leq 100$. Further, the leading term of the shock position series (Equation (A 11b)) comprises λr_i and ct, so that any inaccuracy in r_0 is even less significant in the R_0 term.

A.2 Evaluation of $P_0(m,\tau)$

Substitution of Equation (A8) into Equation (32) yields

$$P_0(m,\tau) = -\frac{\ddot{r}_0}{r_0^2}\left(m + \frac{M_p}{2\pi}\right),$$

*The range of λ is between 1 and 2. The bulk sonic velocity, c, is of the order of 15,000 to 25,000 ft/sec, while v_0 is of the order of 250,000 to 10^6 ft/sec. Hence, c/v_0 may range from about 0.015 to 0.10.

so that, by means of Equation (A14),

$$p_0(m,t) = \frac{3V_0^2}{a^3} g^{-9/4}\left(m + \frac{M_P}{2\pi}\right).$$

Using Equations (7a) and (8), this expression can be put in the form

$$\boxed{p_0(m,t) = \left(\frac{12}{12-3g}\right)\rho^0 V_0^2 g^{-9/4} h^{-9/4}} \qquad (A18)$$

where

$$\boxed{h \equiv 1 + \frac{2\pi m}{M_P} = 1 + \frac{(12-3g)}{4}\frac{m}{\rho^0 a^3}.} \qquad (A19)$$

A.3 Evaluation of $p_0(m,t)$

The leading density coefficient follows directly from Equation (33) once $\theta_0(m)$ is known. This function is derived in precisely the same manner as detailed in Part I, with the exception that now the shock density is allowed to vary. Thus,

$$\theta_0(m) = \theta_0[\tau(m)] = \frac{p_0^*[\tau(m)]^{1/\delta}}{p_0^*[\tau(m)]}, \qquad (A20)$$

where $\tau(m)$ is defined as the time at which the shock front reaches particle m for an impact with $\epsilon \equiv 0$. That is,

$$m(\tau) \equiv \lim_{\epsilon \to 0} m^* = \frac{\rho^0}{3}\left[R_0^3(\tau) - a^3\right]. \qquad (A21)$$

From Equation (A5),

$$\lim_{\epsilon \to 0} p_0^*(\tau) = \frac{\rho^0}{\delta}\left[\dot{R}_0^2(\tau) - c\,\dot{R}_0(\tau)\right]. \qquad (A22)$$

$p_c^*(\tau)$ is obtained as follows.

Substituting Equations (22) and (45) into the right side of Equation (21) yields

$$p^* \rho^{*-\kappa} = \left(\frac{\rho^\circ \gamma^2}{1-\epsilon}\right)\left(\frac{\rho^\circ}{\epsilon}\right)^{-\kappa}$$

or

$$\rho^* = \frac{p^{*1/\kappa}}{\epsilon}\left[\rho^\circ\left(\frac{1-\epsilon}{\rho^\circ \gamma^2}\right)^{1/\kappa}\right] \equiv \frac{p^{*1/\kappa}}{\epsilon} b(\epsilon), \qquad (A23)$$

where

$$b(\epsilon) = \rho^\circ\left(\frac{1-\epsilon}{\rho^\circ \gamma^2}\right)^{1/\kappa}. \qquad (A24)$$

It is assumed that Equation (A23) can be expanded as

$$\frac{\rho_0^*}{\epsilon} + \rho_1^* + \rho_2^* \epsilon + \cdots = \frac{(\rho_0^* + \rho_1^* \epsilon + \cdots)^{1/\kappa}}{\epsilon}(b_0 + b_1 \epsilon + \cdots) \qquad (A25)$$

$$b(\epsilon) = b_0 + b_1 \epsilon + \cdots . \qquad (A26)$$

Taking the limit of Equation (A25) as $\epsilon \to 0$, it follows that

$$\lim_{\epsilon \to 0} \rho_0^* = \lim_{\epsilon \to 0} p_0^{*1/\kappa} b_0 = \left\{\frac{\rho^\circ}{g}\left[\dot{R}_\circ^2(T) - c\dot{R}(T)\right]\right\}^{1/\kappa} b_0, \qquad (A27)$$

where, from Equation (A25),

$$b_0 = \rho^{\circ\frac{\kappa-1}{\kappa}} v_0^{-2/\kappa}. \qquad (A28)$$

Combining Equations (A20), (A22) and (A27), there results

$$\theta_0[\tau(m)] = \frac{1}{b_0}\left\{\frac{\rho^\circ}{g}\left(\dot{R}_\circ^2[\tau(m)] - c\dot{R}_\circ[\tau(m)]\right)\right\}^{\frac{\kappa-\gamma}{\kappa\gamma}}. \qquad (A29)$$

To evaluate Equation (A29) it is simpler to work in terms of $g(\tau)$ and $h(g)$. Thus, from Equations (A11b) and (A14), the term in brackets is

$$\frac{\rho^\circ}{\delta}\left[\dot{R}_o^2(\tau) - c\dot{R}_o(\tau)\right] = \rho^\circ(\delta \dot{r}_o^2 + c\dot{r}_o)$$

$$= \rho^\circ\left[\delta v_o^2 g^{-3/2}(\tau) + c v_o g^{-3/4}(\tau)\right]. \qquad (A30)$$

Again from Equation (A11b) and the definition of g,

$$\frac{R_o}{a} = \delta g^{1/4} + \frac{1}{4}\left(\frac{c}{v_o}\right) g - \left(\frac{1}{4}\left(\frac{c}{v_o}\right) + \delta - 1\right). \qquad (A31)$$

Hence, Equation (A21) can be written as

$$m(\tau) = \frac{\rho^\circ a^3}{3}\left\{\frac{R_o^3[g(\tau)]}{a^3} - 1\right\},$$

or

$$\frac{m}{\rho^\circ a^3}(g) \equiv \frac{1}{3}\left[\frac{R_o^3(g)}{a^3} - 1\right].$$

Lastly, from the definition of h, Equation (A19),

$$\frac{m}{\rho^\circ a^3} = \frac{4}{12 - 3\delta}(h - 1),$$

so that

$$h = \frac{12 - 3\delta}{4}\left(\frac{m}{\rho^\circ a^3}\right) + 1$$

and,

$$h(g) \equiv h[m(g)] = \frac{12 - 3\delta}{12}\left\{\left[\frac{R_o(g)}{a}\right]^3 - 1\right\} + 1. \qquad (A32)$$

*Note, h(g) is analagous to $m(\gamma)$. Thus, g(h) is defined as the generalized time (g) at which the shock front reaches particle $h = \frac{12-3\delta}{4}\left(\frac{m}{\rho^\circ a^3}\right)+1$, for an impact with $\epsilon \approx 0$.

The function obtained by solving Equation (A32) for g as a function of h, i.e., g(h), is then substituted into Equation (A30) to obtain the desired function of h and thus m.

Equation (A32) is shown plotted in Figure (A3) for the two bounding cases of (α, c/v_0). As can be seen, the curves differ from each other but each approximates $g^{3/5}$ behavior for moderate values of g.* Further, since Equation (A30) must be raised to the $\frac{\kappa-\gamma}{\kappa\gamma}$ power (see Equation (A29)), which is generally of the order of 0.1, any deviation from $g^{3/5}$ behavior is minimized. For example, if the expression given by Equation (A30) were off by as much as a factor of 2** the resultant error in $\theta_0(m)$ as given by Equation (A29) would by only 7%. Hence, it is possible to represent g(h) simply as

$$g(h) = h^{5/3} \qquad (A33)$$

without introducing any significant error into the analysis. The factor 5 varies with (α, c/v_0) as illustrated in Figure 5. The values of 5 for the two limiting cases follows directly from the approximating straight lines depicted in Figure A3. Intermediate value curves are approximated in the same manner and corresponding values of 5 evaluated.

---

* This form is suggested by Equations (A31) and (A32). For small g, $R_{o/a} \propto g^{1/4}$ and $h \propto g^{3/4}$. For large g, $R_{o/a} \propto g$, and $h \propto g^3$. Thus, h ranges from $g^{3/4}$ to $g^{3/1}$ behavior as g increases. Hence, 5 is never truly a constant. However, for the range of g of interest, $g^{3/5}$ is a good representation of h(g). Of course, 5 is a function of α and c/v_0.

**A deviation of this magnitude could occur only at g values of 100 or greater and at the extreme of the α, c/v_0 range. For most substances and for g values up to 100, the deviations are generally much less.

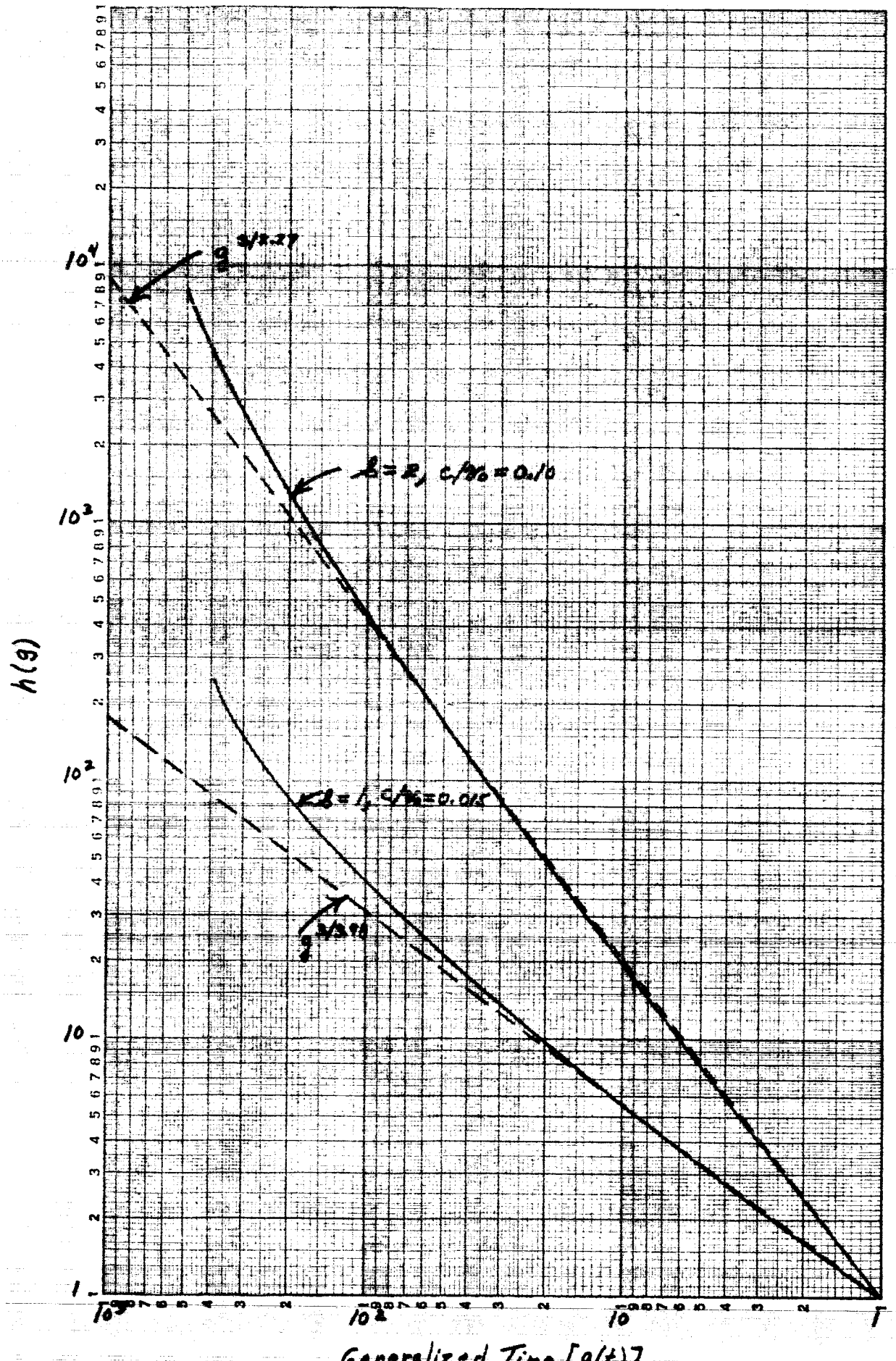

Fig. A3. The "3/t" approximation for h(g)

From Equations (A29), (A28), (A30), and (A33), it follows that

$$\theta_0(m) = v_0^{2/\kappa} \rho^{0\,(1-\gamma)/\gamma} \left[\tfrac{1}{2}\gamma_0 v_0^2 h^{-5/2} + c v_0 h^{-5/4} \right]^{\frac{\kappa-\gamma}{\kappa\gamma}} . \tag{A34}$$

Hence, combining Equations (33), (A18) and (A34),

$$\rho_0(m,t) = \rho^0 \left(\frac{12}{12-3\beta}\right)^{1/\gamma} \left(\frac{v_0}{c}\right)^{\frac{\kappa-\gamma}{\kappa\gamma}} g^{-9/4\delta} \left(\frac{h^{5/4}}{\frac{1}{2}\frac{\gamma_0}{c} h^{-5/4} + 1} \right)^{\frac{\kappa-\gamma}{\kappa\gamma}} h^{1/\gamma} . \tag{A35}$$

A.4 Evaluation of $r_1(m,t)$

Reference to Equation (34) shows that once $r_1(0,t) = X_1(t)$ (see Equation (38b)) is specified, $r_1(m,t)$ is determinate. The procedure for evaluating X_1 is identical to that for r_0.

Equation (35) evaluated at the shock as $\epsilon \to 0$ yields, using Equation (34) for $r_1(m,t)$ and Equations (A3) and (A4),

$$p_1(0,t) = \frac{\rho^0}{\delta}\left(2\dot{R}_0\dot{R}_1 - c\dot{R}_1\right) - 2\frac{\ddot{r}_0}{r_0^3}\underbrace{\int_0^{\frac{\rho^0}{3}(R_0^3-a^3)} \left[\int_0^m \frac{dm}{\rho_0 r_0^2} + X_1 \right] dm}_{I_1^*} + \underbrace{\frac{1}{r_0^2}\int_0^{\frac{\rho^0}{3}(R_0^3-a^3)} \frac{\partial^2}{\partial t^2}\left[\int_0^m \frac{dm}{\rho_0 r_0^2} + X_1 \right] dm}_{I_2^*} . \tag{A36}$$

From the target-modified-penetrator interface condition, Equation (A7), and Equation (A8), a second expression for $p_1(0,t)$ is

$$p_1(0,t) = \frac{M_2}{2\pi}\left(\frac{-\ddot{X}_1}{2r_0^2} + \frac{\ddot{r}_0 X_1}{r_0^3} \right) . \tag{A37}$$

Another expression relating F_1 and X_1 follows from the shock velocity condition evaluated as $\epsilon \to 0$. Thus, from Equation (A9)

$$\lim_{\epsilon \to 0} \left\{ \left.\frac{\partial r_1}{\partial t}\right|_{m,t} \right\} = \frac{\dot{R}_1}{\delta} ,$$

so that

$$\lim_{\epsilon \to 0} \left\{ \frac{\partial r_1}{\partial \epsilon}\Big|_{m^*=\epsilon} \right\} = \lim_{\epsilon \to 0} \left\{ \left(\frac{\partial}{\partial t} \left[\int_0^m \frac{dm}{\rho_0 r_0^2} + X_1 \right] \right)_{m^*=\epsilon} \right\}$$

$$= \lim_{\epsilon \to 0} \left\{ \int_0^{m^*} \frac{\partial}{\partial t} \left(\frac{1}{\rho_0 r_0^2} \right) dm + \dot{X}_1 \right\}$$

$$= \underbrace{\int_0^{\frac{\rho^0}{3}(R_0^3 - a^3)} \frac{\partial}{\partial t} \left(\frac{1}{\rho_0 r_0^2} \right) dm}_{I_3^*} + \dot{X}_1 = \frac{\dot{R}_1}{\delta} . \qquad (A38)$$

Equations (A36), (A37), and (A38) provide two simultaneous differential equations for R_1 and X_1 . Before discussing their solution, the evaluation of integrals I_1^*, I_2^*, and I_3^* is described.

A.4.1. Evaluating the Integrals

The three integrals each require the calculation of

$$\int_0^m \frac{dm}{\rho_0 r_0^2} = \frac{4\rho^0 a^3}{12 - 3q} \int_1^h \frac{dh}{\rho_0 r_0^2} . \qquad (A39)$$

Since r_0 is independent of m and $\rho_0(m,t)$ is separable in m and t , the integration of Equation (A39) is, from Equation (A35),

$$\int_0^m \frac{dm}{\rho_0 r_0^2} \propto \int_1^h h^{-1/6} \left(\frac{h^{3/4}}{\delta \frac{v_0}{c} h^{-3/4} + 1} \right)^{\frac{r-\kappa}{\kappa+r}} dh . \qquad (A40)$$

For arbitrary β, c/v_0, γ and κ this expression is not readily integrable in closed form. However, the term raised to the $\frac{\gamma-\kappa}{\kappa\gamma}$ power is insensitive to variations in β and c/v_0 (which determine f) and can be represented accurately by

$$G^{\frac{\gamma-\kappa}{\kappa\gamma}} \equiv \left(\frac{h^{5/4}}{\beta\frac{v_0}{c}h^{-5/4}+1}\right)^{\frac{\gamma-\kappa}{\kappa\gamma}} = K_2 h^{-\nu}, \qquad (A41)$$

where K_2 and ν vary only with $\frac{\gamma-\kappa}{\kappa\gamma}$. Figure A4 shows the variation of $G^{\frac{\gamma-\kappa}{\kappa\gamma}}$ with h for a wide range of β, c/v_0 values. As can be seen, the large variation in β, c/v_0 causes little spread in the curves which are well represented by $K_2 h^{-\nu}$. The varia tion of K_2 and ν with $\frac{\kappa-\gamma}{\kappa\gamma}$ is shown in Figure 6.

With this simplification, the integral of Equation (A40) follows as

$$\int_1^h h^{-\frac{1}{\gamma}} G^{\frac{\gamma-\kappa}{\kappa\gamma}} = K_2 \int_1^h h^{-\frac{1}{\gamma}} h^{-\nu} = K_2 \left(\frac{\gamma_1}{\gamma_1-1}\right)\left(h^{\frac{\gamma_1-1}{\gamma_1}}-1\right), \qquad (A42)$$

where

$$\frac{1}{\gamma_1} \equiv \frac{1}{\gamma} + \nu. \qquad (A43)$$

The other operations involved in I_1, I_2, and I_3 are straightforward.* The results are

$$I_1^* = -6\frac{v_0^2}{a^4} g^{-2.5}\left(\mathbb{D} J_2 g^{\frac{1}{4}\left(\frac{9}{\gamma}-2\right)} + \frac{4\rho^0 a^3 \chi_1}{12-3g}\left[g^{\frac{3}{5}}-1\right]\right) \qquad (A44)$$

---

* To carry out the integrations, it is expedient to change the variable of integration from m to h. In so doing, m (τ) is replaced by h (g), where the approximation (see Equation (A33))

$$h(g) \equiv h[m(g)] = g^{3/5}$$

is used.

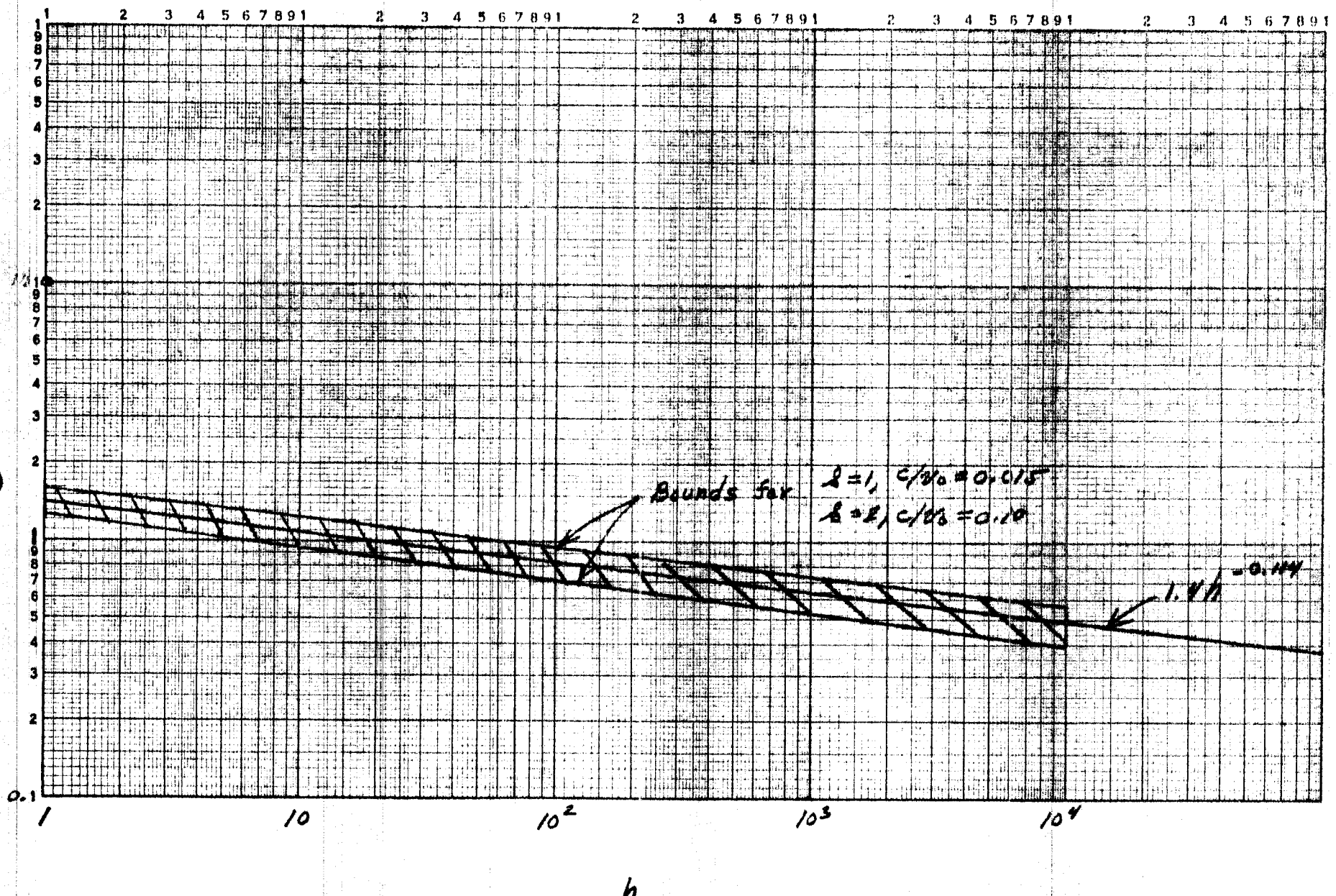

Fig. A4. Approximating $G^{(\alpha-\gamma)}_{rr}$ by $K_2 h^{-\nu}$

$$I_2^* = \frac{\gamma_0^2}{r_0^2 a^2}\left(\frac{9}{8}-2\right)\left(\frac{9}{8}-6\right)\mathbb{D}\,J_2\,g^{\frac{1}{4}\left(\frac{9}{8}-10\right)} + \frac{4P^\circ a^3}{(12-3g)\,r_0^2}\ddot{X}_1\left(g^{3/5}-1\right) \qquad (A45)$$

$$I_3^* = \left(\frac{\gamma_1}{\gamma_1-1}\right)\left(\frac{9}{8}-2\right)\frac{\gamma_0}{a}K_2\,\mathbb{D}\,g^{\frac{1}{4}\left(\frac{9}{8}-6\right)}\left[g^{\frac{3}{5}\left(\frac{\gamma_1-1}{\gamma_1}\right)}-1\right], \qquad (A46)$$

where

$$J_2 \equiv \frac{4P^\circ a^3 K_2}{12-3g}\,\frac{\gamma_1^2}{(\gamma_1-1)(2\gamma_1-1)}\left(h^{*\frac{2\gamma_1-1}{\gamma_1}}\,\frac{2\gamma_1-1}{\gamma_1}\,h^* + \frac{\gamma_1-1}{\gamma_1}\right)$$

$$\mathbb{D} \equiv \frac{4a}{(12-3g_0)}\left(\frac{12}{12-3g}\right)^{-1/8}\left(\frac{\gamma_0}{c}\right)^{\frac{8-\gamma}{5\gamma}}.$$

A.4.2 Solving for X_1 & R_1

Substituting for $\dot{R}_1$ by means of Equation (A38) yields a differential equation for X_1:

$$\frac{M_p}{\pi}\left(\frac{-\ddot{X}_1}{2r_0^2} + \frac{\ddot{r}_c}{r_0^3}X_1\right) = P^\circ\left(2\dot{R}_0 - c\right)\left(I_3 + \dot{X}_1\right) - I_1^* + I_2^*. \qquad (A47)$$

Substituting for $\dot{R}_0$ and r_c and its derivatives (see Equations (A10) and (A14)), and using the integral expressions, Equations (A44), (A45), and (A46), this equation reduces to

$$\left[\frac{4P^\circ a}{12-3g}g^{\left(\frac{3}{5}-\frac{1}{2}\right)}\right]\ddot{X}_1 + \left[P^\circ\left(c + 2\left(\frac{\gamma_0}{g}\right)^{3/4}\right)\right]\dot{X}_1 +$$

$$\left[\frac{24P^\circ v_3^2}{(12-3g)\,a}\,g^{\frac{3}{5}-\frac{5}{2}}\right]X_1 = f_1(g), \qquad (A48)$$

where

$$f_1(g) \equiv I_1^* - \left[\frac{24\rho^\circ v_0^2}{(12-3g)a}(1-g^{3/5})g^{-5/2}\right]X_1 + I_2^* - \left[\frac{4\rho^\circ a}{12-3g}(1-g^{3/5})g^{-1/2}\right]\dot{X}_1 - I_3^*\rho^\circ(c+2\ell v_0 g^{-3/4}). \quad (A49)$$

Equation (A48) can be simplified by changing the independent variable from t to g, i.e.,

$$\dot{X}_1 = \frac{dX}{dg}\frac{dg}{dt} \equiv X_1'\frac{4v_0}{a} \quad (A50a)$$

$$\ddot{X}_1 = X_1''\frac{16v_0^2}{a^2}, \quad (A50b)$$

and dividing by

$$\frac{4\rho^\circ v_0^2}{(12-3g)a}g^{3/5-5/2}.$$

Thus,

$$16g^2X_1'' + \left[(12-3g)g^{\frac{5}{2}-\frac{3}{5}}\left(\frac{c}{v_0}+2\ell g^{-3/4}\right)\right]X_1' + 6X_1 = \frac{(12-3g)a\,f_1(g)}{4\rho^\circ v_0^2 g^{3/5-5/2}} \equiv f_2(g). \quad (A51)$$

If the coefficient of X_1' is proportional to g, Equation (A51) takes the form of the equidimensional linear equation or Cauchy's equation and is readily solved. This is indeed the case, as is illustrated in Figure A5, where the expression

$$\frac{c}{v_0}g^{5/2-3/5} + 2\ell g^{7/4-3/5}$$

is plotted as a function of g for the limiting cases of $\ell, c/v_0$. Hence, it is possible to replace the multiplier of X_1' by $4K_3 g$ without introducing any significant

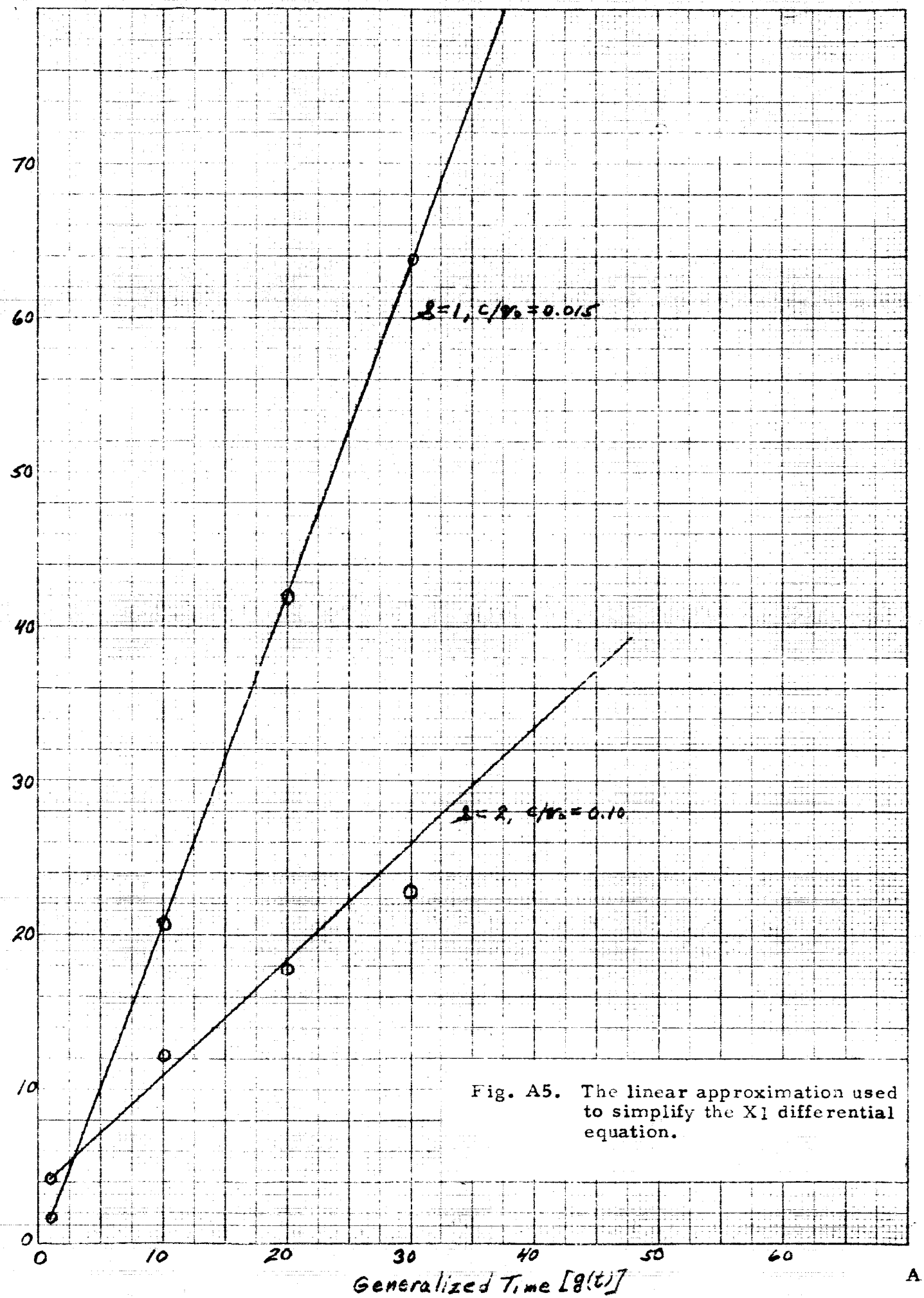

Fig. A5. The linear approximation used to simplify the X1 differential equation.

error into the analysis over the range of g of physical interest.

Thus,

$$(12-3g)\left(\frac{c}{v_0}g^{5/2-3/5} + 2\delta g^{7/4-3/5}\right) \simeq (12-3g)K_3' g \equiv 4K_3 g \qquad (A52)$$

or

$$K_3 = \frac{12-3g}{4} K_3', \qquad (A53)$$

where the variation of K_3' with $\delta, c/v_0$ is shown in Figure 7.

With the preceding simplification, the differential equation becomes

$$16 g^2 X_1'' + 4K_3 g X_1' + 6X_1 = f_2(g), \qquad (A54)$$

a form which readily yields an analytical solution. Thus, for the appropriate boundary conditions (see Equations (14) and (15)),

$$X_1(0) = 0 \qquad (A55a)$$

$$\dot{X}_1(0) = v_1, \qquad (A55b)$$

the solution of Equation (A54) is

$$\boxed{\frac{X_1}{a} = g^{\omega_R}\left[C_1 \cos(\omega_I \ln g) + C_2 \sin(\omega_I \ln g)\right] + \sum_{i=1}^{7} \mathcal{L}_i g^{l_i}} \qquad (A56)$$

where the constants $\omega_R, \omega_I, C_1, C_2$ and the $\mathcal{L}_i$'s and the l_i's are defined as follows:

1. ω_R & ω_I

$$\omega_R \equiv \frac{1}{2}(1 - 0.25K_3) \qquad (A57a)$$

$$\omega_I \equiv \left(0.375 - \omega_R^2\right)^{1/2} \qquad (A57b)$$

2. l_i

$$l_1 \equiv \frac{3}{5} - 0.5 + \frac{2}{\gamma} - \frac{3}{5\gamma_1} + \frac{0.25}{\gamma} \qquad (A58a)$$

$$l_2 \equiv -0.5 + \frac{2}{\gamma} + \frac{0.25}{\gamma} \qquad (A58b)$$

$$l_3 \equiv \frac{2}{\gamma} - \frac{3}{5\gamma_1} + \frac{0.25}{\gamma} + 1 \qquad (A58c)$$

$$l_4 \equiv -\frac{3}{5} + 0.25 + \frac{2}{\gamma} + \frac{0.25}{\gamma} \qquad (A58d)$$

$$l_5 \equiv -\frac{3}{5} - 0.5 + \frac{2}{\gamma} + \frac{0.25}{\gamma} \qquad (A58e)$$

$$l_6 \equiv -\frac{3}{5} + \frac{2}{\gamma} + \frac{0.25}{\gamma} + 1 \qquad (A58f)$$

$$l_7 \equiv 0.25 + \frac{2}{\gamma} - \frac{3}{5\gamma_1} + \frac{0.25}{\gamma} \qquad (A58g)$$

3. $\mathcal{L}_i$

$$\mathcal{L}_i \equiv \frac{i}{16} \frac{L_i}{l_i^2 - (1 - 0.25K_3)l_i + 0.375} \qquad (A59)$$

$$L_1 \equiv -\frac{\gamma_1}{\gamma_1 - 1}\beta \qquad (A60a)$$

$$L_2 \equiv \frac{(2\gamma_1 - 1)}{\gamma_1}\beta \qquad (A60b)$$

$$L_3 \equiv -\delta \qquad (A60c)$$

$$L_4 \equiv 2\beta\left(\frac{v_0}{c}\right)\delta \qquad (A60d)$$

$$L_5 \equiv -\beta \qquad (A60e)$$

$$L_6 \equiv \delta \qquad (A60d)$$

$$L_7 \equiv -2\beta\left(\frac{v_0}{c}\right)\delta \qquad (A60e)$$

and

$$\beta \equiv \frac{1}{3} K_2 \left[\frac{12}{12-3g}\right]^{\frac{\gamma-1}{\gamma}} \left(\frac{v_0}{c}\right)^{\frac{\gamma-\gamma_1}{\gamma\gamma}} \left(\frac{\gamma_1}{2\gamma_1-1}\right)\left[6+\left(\frac{q}{\gamma}-2\right)\left(\frac{q}{\gamma}-6\right)\right] \quad (A61)$$

$$\delta \equiv \left(\frac{12}{12-3g}\right)^{-1/\gamma} K_2 \left(\frac{v_0}{c}\right)^{\frac{\gamma-\gamma_1}{\gamma\gamma}} \left(\frac{\gamma_1}{\gamma_1-1}\right)\left(\frac{q}{\gamma}-2\right) \quad (A62)$$

4. $\underline{C_i}$

$$C_1 \equiv -\sum_{i=1}^{7} \mathcal{L}_i \quad (A63a)$$

$$C_2 = \frac{1}{\omega_L}\left\{0.25a\left(\frac{v_1}{v_0}\right) + \sum_{i=1}^{7} \mathcal{L}_i(\omega_R - \lambda_i)\right\}. \quad (A63b)$$

R_i follows directly from Equations (A38) and (A46) as, since $R_1(0)=0$,

$$\boxed{\frac{R_1}{a} = \delta\left\{\frac{X_1}{a} + \left(\frac{v_0}{c}\right)\frac{\delta}{(12-3g)}\left[\frac{g^{\lambda_1}-1}{\lambda_1} - \frac{(g^{\lambda_2}-1)}{\lambda_2}\right]\right\}.} \quad (A64)$$

A.4.3 Calculating $r_1(m,t)$

Using Equations (A42), (A35), and (A39), the expression for $r_1(m,t)$, Equation (34), reduces to

$$r_1(m,t) = \frac{4a\kappa_2}{(12-3\beta)}\left(\frac{c}{V_0}\right)^{\frac{\kappa-\gamma}{\kappa\gamma}}\left(\frac{12}{12-3\beta}\right)^{-1/\gamma}\left(\frac{\gamma_1}{\gamma_1-1}\right)g^{\left(\frac{9}{4\gamma}-\frac{1}{2}\right)}\left(h^{\frac{\gamma_1-1}{\gamma_1}}-1\right)+X_1, \qquad (A65)$$

where $X_1(t)$ is given by Equation (A56).

A.5 Evaluation of $p_1(m,t)$

This coefficient comprises two terms (see Equation (35)). From Equation (A36),

$$p_1(0,t) = \frac{\rho^\circ}{g}\left(2\dot{R}_0\dot{R}_1 - c\dot{R}_1\right) - I_1^* + I_2^*$$

where I_1^* and I_2^* are given by Equations (A44) and (A45). The second term of $p_1(m,t)$ is

$$\underbrace{\frac{2\ddot{r}_0}{r_0^3}\int_0^m r_1\,dm}_{I_1} - \underbrace{\frac{1}{r_0^2}\int_0^m \frac{\partial^2 r_1}{\partial t^2}\,dm}_{I_2},$$

where

$$I_1 = -\frac{6v_0^2}{a^4} g^{-2.5} \left(\mathbb{D} J_2' g^{\frac{1}{4}\left(\frac{9}{\gamma}-2\right)} + X_1 m \right) \qquad (A66)$$

$$I_2 = \frac{v_0^2}{r_0^2 a^2} \left(\frac{9}{\gamma}-2\right)\left(\frac{9}{\gamma}-6\right) \mathbb{D} J_2' g^{\frac{1}{4}\left(\frac{9}{\gamma}-10\right)} + \ddot{X}_1 m ; \qquad (A67)$$

$$J_2' \equiv \frac{4\rho^0 \Omega^3 K_2}{(12-3\gamma)} \left(\frac{\gamma_1^2}{[\gamma_1-1][2\gamma_1-1]} \right) \left(h(m)^{\frac{2\gamma_1-1}{\gamma_1}} - \frac{(2\gamma_1-1)}{\gamma_1} h(m) + \frac{\gamma_1-1}{\gamma_1} \right). \qquad (A68)$$

Hence,

$$\boxed{P_1(m,t) = (I_1 - I_1^*) - (I_2 - I_2^*) + \frac{\rho^0}{g} (2\dot{R}_0 \dot{R}_1 - c\ddot{R}_1).} \qquad (A69)$$